Foldamers rescue synucleinopathy phenotypes in multiple in vitro and in vivo models

Ryan A. Dohoney[1,2]† , L. Palanikumar[3]†, Emily Oldani[1,2,4]†, Charles Zuwu Baysah[1,2], Johnson A. Joseph[1,2], David Polanco[5], Paula Santos-Otte[6], Nicholas H. Stillman[1,2], Peter Corcoran[1,2,4], Tyler D. Ball[1,2], Tessa C. Fitch[2], Jemil Ahmed[2,3], Ifunayachi Ogbonna-Ukuku[1,2], Kevin M. Reynolds Caicedo[2,7], Ying Liu[8], Maureen A. Leehey[8], Daniel A. Linseman[2,4,7], Daniel A. Paredes[2,9], Melissa Birol[6], Nunilo Cremades[5], Mazin Magzoub[3]*, Sunil Kumar[1,2,4]*

Synucleinopathies is an umbrella term for multiple neurological disorders, including Parkinson's disease (PD), Lewy body dementia (LBD), and multiple system atrophy (MSA). A central pathological hallmark of synucleinopathies is the aggregation of α-synuclein (αS, a neuronal protein) and its prion-like spread. Therefore, inhibition of αS aggregation and spread is considered a viable therapeutic approach for the treatment of synucleinopathies. Foldamers are synthetic ligands that mimic the secondary structure of proteins. Using an oligoquinoline (OQ) scaffold–based foldamer approach, we have previously identified a foldamer (SK-129) that potently inhibits αS aggregation. Here, using a wide range of biophysical, cellular, and in vivo methods, we showed that SK-129 rescued synucleinopathy phenotypes in cellular, Caenorhabditis elegans, and human induced pluripotent stem cell (iPSC)– derived neuron models. SK-129 specifically bound to neurotoxic αS oligomers with ~6-fold higher affinity (Kd = 221 ± 29 nM) than to physiological αS monomer, validating αS oligomers as a therapeutic target. Furthermore, SK-129 efficiently crossed the blood-brain barrier (BBB) and exhibited favorable pharmaceutical properties in mice. Treatment with SK-129 prevented brain histopathology and increased survival in a mouse model expressing human A53T mutant αS without showing any apparent cytotoxicity. SK-129 inhibited αS aggregation mediated by exosomes derived from C. elegans or patients with PD in HEK293T reporter cells. SK-129 completely inhibited the coaggregation of αS-tau, a pathological biomarker for LBD in both cellular and mouse models. Overall, we report a potent foldamer with therapeutic potential for PD and LBD.

INTRODUCTION

αS is a highly expressed neuronal protein in dopaminergic (DA) neurons and plays a key role in synaptic vesicle trafficking, recycling, and neurotransmitter release (*1*–*3*). Abnormal aggregation of αS underlies a group of neurodegenerative disorders, including Parkinson's disease (PD), Lewy body dementia (LBD), and multiple system atrophy (MSA), collectively termed synucleinopathies (*4*). The αS aggregation proceeds through the formation of pathological oligomers and ultimately insoluble fibers, leading to DA neuron dysfunction, a central pathophysiological event in synucleinopathies (*1*–*3*). Oligomers are considered as the most neurotoxic conformation of αS and induce cellular damage through multiple mechanisms (*5*, *6*). In addition, the depletion of functional monomeric αS due to aggregation impairs dopamine trafficking and release, further contributing to PD progression (*7*). The pathological αS aggregates can propagate between neurons via a prion-like mechanism, templating soluble αS into insoluble aggregates (*1*–*3*). Also, increasing evidence indicates that coaggregation of αS with tau is a key pathological feature of synucleinopathies (*8*–*14*). Tau, a microtubule-associated protein implicated in Alzheimer's disease (AD) and synucleinopathies (*15*–*18*), is present as pathological aggregates in ~50% of patients with PD (*8*–*10*). Coexisting αS and tau pathologies exacerbate both motor and cognitive deficits, highlighting their importance as therapeutic targets (*8*–*10*). Additional copathologies involving αS with amyloid-β (Aβ) or TAR DNA-binding protein 43 (TDP-43) further contribute to disease heterogeneity (*8*–*10*, *19*, *20*). Collectively, synucleinopathies arise from multiple pathogenic processes, including αS aggregation, toxic oligomer formation, prion-like spread, and coaggregation with tau, Aβ, or TDP-43 (*8*–*10*, *19*, *20*). Therapeutic strategies that modulate these interconnected pathways may therefore offer disease-modifying potential (*5*, *6*, *21*–*28*).

Although numerous ligands have been reported to inhibit αS aggregation and rescue disease phenotypes (*5*, *6*, *21*–*28*), most have not advanced to clinical trials. The major limitations include selective modulation of only a single toxic pathway, poor pharmaceutical properties, limited blood-brain barrier (BBB) penetration, and incomplete understanding of their mechanisms of action. Notably, no ligand has been reported to inhibit αS-tau coaggregation. Consequently, there are currently no effective disease-modifying therapies for synucleinopathies (*5*, *6*, *21*–*30*). Ligands capable of targeting multiple pathogenic mechanisms while exhibiting favorable pharmaceutical properties would represent promising therapeutic candidates.

[1]Department of chemistry and Biochemistry, F. W. olin hall, 2190 e. iliff Ave., University of Denver, Denver, co 80210, USA.[2]Knoebel institute for healthy Aging, 2155 e. Wesley Ave., Suite 579, University of Denver, Denver, co 80208, USA.[3]Biology Program, Division of Science, new York University Abu Dhabi, Po Box 129188, Saadiyat island, Abu Dhabi, United Arab emirates.[4]Molecular and cellular Biophysics Program, Boettcher West, room 228, 2050 e. iliff Ave., University of Denver, Denver, co 80210, USA.[5]institute for Biocomputation and Physics of complex Systems (BiFi) and Department of Biochemistry and Molecular and cellular Biology, University of Zaragoza, Zaragoza 50009, Spain.[6]Max Delbrück center for Molecular Medicine, Berlin institute for Medical Systems Biology, Berlin 10115, Germany.
[7]Department of Biological Sciences, F. W. olin hall, 2190 e. iliff Ave., University of Denver, Denver, co 80210, USA.[8]Department of neurology, University of colorado Anschutz Medical campus School of Medicine, Aurora, co 80045, USA.[9]ritchie School of engineering and computer Science, 2155 e. Wesley Ave., University of Denver, Denver, co 80210, USA.
*corresponding author. email: sunil.kumar97@du.edu (S.K.); mazin.magzoub@nyu.edu (M.M.)
†These authors contributed equally to this work.

To address these challenges, we used an oligoquinoline (OQ) scaffold–based foldamer approach to identify potent antagonists of αS aggregation. OQs are synthetic foldamers that present chemically diverse side chains capable of mimicking protein secondary structural interfaces involved in aggregation (*24*, *31*–*33*). OQ foldamers have been shown to inhibit aggregation of multiple amyloid proteins, and their side chain diversity can be synthetically tuned to optimize target interactions (*24*, *31*–*33*). Using this approach, we previously identified SK-129 as a potent antagonist of αS aggregation. SK-129 binds the N terminus of αS by interacting with four sequence regions (residues 6 to 12, 15 to 23, 36 to 45, and 48 to 53) and inhibits αS aggregation in biophysical, cellular, and *Caenorhabditis elegans* models (*24*). Here, we have evaluated its antagonist activity against αS and αS-tau aggregation, pharmaceutical properties, BBB penetration and exposure, and efficacy in mice disease models. Overall, this study identified lead therapeutics for synucleinopathies, which could aid in developing promising disease modifying therapies for synucleinopathies.

RESULTS

SK-129 rescues the degeneration of DA neurons

We tested the efficacy of SK-129 in inhibiting intraneuronal αS aggregation in DA neurons using UA196 worms, a well-established PD model (Fig. 1, A and B) (*21*, *28*, *34*–*36*). UA196 worms simultaneously express human αS and green fluorescent protein (GFP) in six DA neurons located in the anterior region (*21*, *28*, *34*–*36*). During aging, αS aggregation induces progressive DA neuron degeneration, as previously reported (*21*, *28*, *34*–*36*). The neurodegeneration was characterized by a time-dependent loss of DA neuron cell bodies from day 3 to day 15 (Fig. 1, C to H), accompanied by neurite fragmentation and blebbing (*21*, *28*, *34*–*36*). Each biological replicate consisted of 10 worms (six DA neurons per worm; total = 60 neurons). The average number of healthy DA neurons declined from 59 on day 3 to 42.1, 20.5, and 15.2 on days 5, 10, and 15, respectively (Fig. 1I). To assess neuroprotection, UA196 worms were treated with SK-129 (50 μM) on days 2 and 4 (Fig. 1A). In the presence of SK-129, the numbers of healthy DA neurons were 58.2, 56.8, and 56.5 on days 5, 10, and 15, respectively (Fig. 1I, orange; Fig. 1, J and K). SK-129 rescued DA neuron degeneration in a dose-dependent manner (Fig. 1I) and remained chemically intact in *C. elegans*, as confirmed by high-resolution mass spectrometry (HRMS) (Fig. 1L). Compared with literature-reported ligands targeting PD, SK-129 was more effective in rescuing DA neuron degeneration in UA196 worms (Fig. 1M). On day 15, treatment with bexarotene (*37*), tyrosol (*38*), valproic acid (*39*), and epigallocatechin gallate (EGCG) (*40*) (50 μM each) yielded 22.5, 25.5, 22.5, and 34.5 healthy neurons, respectively, with EGCG showing only moderate efficacy (Fig. 1M).

Treatment of UA196 worms with SK-129 rescues motility

The degeneration of neurons in UA196 worms is associated with impaired motor function and reduced motility (*2*, *3*, *7*, *28*, *34*, *41*). We assessed the effect of SK-129 on worm motility using a WMicroTracker ARENA plate reader (*42*). The UA196 worms were treated with 50 μM SK-129 on days 2 and 4, and motility was compared with healthy N2 controls (Fig. 1, N and O). As expected, the motility of untreated UA196 worms declined with age relative to N2 controls (Fig. 1, N and O). In contrast, SK-129 treatment markedly improved motility and restored activity to levels comparable to those of N2 worms (Fig. 1, N and O).

Attenuation of ROS by SK-129 in UA196 worms

The generation of reactive oxygen species (ROS) drives lipid, protein, and DNA oxidation, and it is closely linked to PD pathogenesis (*28*, *34*, *41*). In UA196 worms, αS aggregation enhances ROS production, which was quantified using the fluorescent probe CM-H2DCFDA, as previously described (*28*, *35*, *36*). Upon reaction with ROS, probe fluorescence increased over a 2-hour period in untreated UA196 worms (Fig. 1P). In contrast, treatment with SK-129 (50 μM on days 2 and 4) resulted in the reduction in ROS-dependent fluorescence intensity (Fig. 1P). This decrease in ROS levels is consistent with inhibition of intracellular αS aggregation by SK-129.

SK-129 rescues behavioral deficits in UA196 worms

The degeneration of DA neurons reduces dopamine levels and leads to behavioral deficits in *C. elegans*, including impaired food-sensing behavior (*28*, *34*, *42*, *43*). To test whether SK-129 rescues behavioral deficits in UA196 worms, we used a well-established chemotaxis assay (*28*, *34*, *42*, *43*). In this assay, worms distinguish food (*Escherichia coli*) as an attractant from ethanol as a repellent. The behavioral performance of UA196 worms treated with SK-129 (±50 μM on days 2 and 4) was compared with untreated UA196 and healthy N2 worms on days 3 and 10. The worms were placed at the center of plates containing two quadrants with *E. coli* and two with ethanol (Fig. 1Q), and a chemotaxis index (CI; range −1 to +1) was measured over time using the ARENA plate reader. On day 3, UA196 (±SK-129) and N2 worms showed no behavioral deficits, with CI values of ~1 for *E. coli* and ~−1 for ethanol, indicating strong attractant preference (Fig. 1R and fig. S1, A to C). By day 10, untreated UA196 worms displayed CI values near zero, indicating the loss of preference and behavioral impairment (Fig. 1S and fig. S1E). In contrast, SK-129–treated UA196 worms retained CI values of ~1 (*E. coli*) and ~−1 (ethanol) comparable to N2 controls (Fig. 1S and fig. S1, D and F). Collectively, SK-129 rescued both neurodegeneration and behavioral deficits in UA196 worms.

SK-129 enhances dopamine in UA196 worms

Neurodegeneration in UA196 worms is associated with impaired motility resulting from reduced dopamine levels (*28*, *34*, *41*). We therefore hypothesized that motility deficits could be rescued by exogenous dopamine. UA196 worms were treated with 2 mM dopamine (±50 μM SK-129 on days 2 and 4), and their motility was compared with N2 worms treated with dopamine under identical conditions. As expected, dopamine treatment did not alter motility in N2 worms, likely because of intact DA neuron function (Fig. 2A). In contrast, dopamine improved motility in UA196 worms, consistent with compensation by exogenous dopamine (Fig. 2B). Notably, UA196 worms treated with SK-129 did not show further motility enhancement upon dopamine supplementation, consistent with rescue of DA neuron degeneration and restoration of endogenous dopamine synthesis (Fig. 2C).

Treatment with SK-129 reduces neurodegeneration and ROS production in a postdisease PD model

SK-129 potently rescued DA neurons and PD phenotypes in UA196 worms when administered at early disease stages, mimicking a preventative strategy. However, because current PD therapies are typically applied after diagnosis (*28*, *36*), we next evaluated SK-129 in a postdisease model. A loss of ~30% DA neurons by day 5 has been established as a postdisease time point in UA196 worms (*28*, *36*). Accordingly, UA196 worms were treated with SK-129 on day 5 (Fig. 2, D and E).

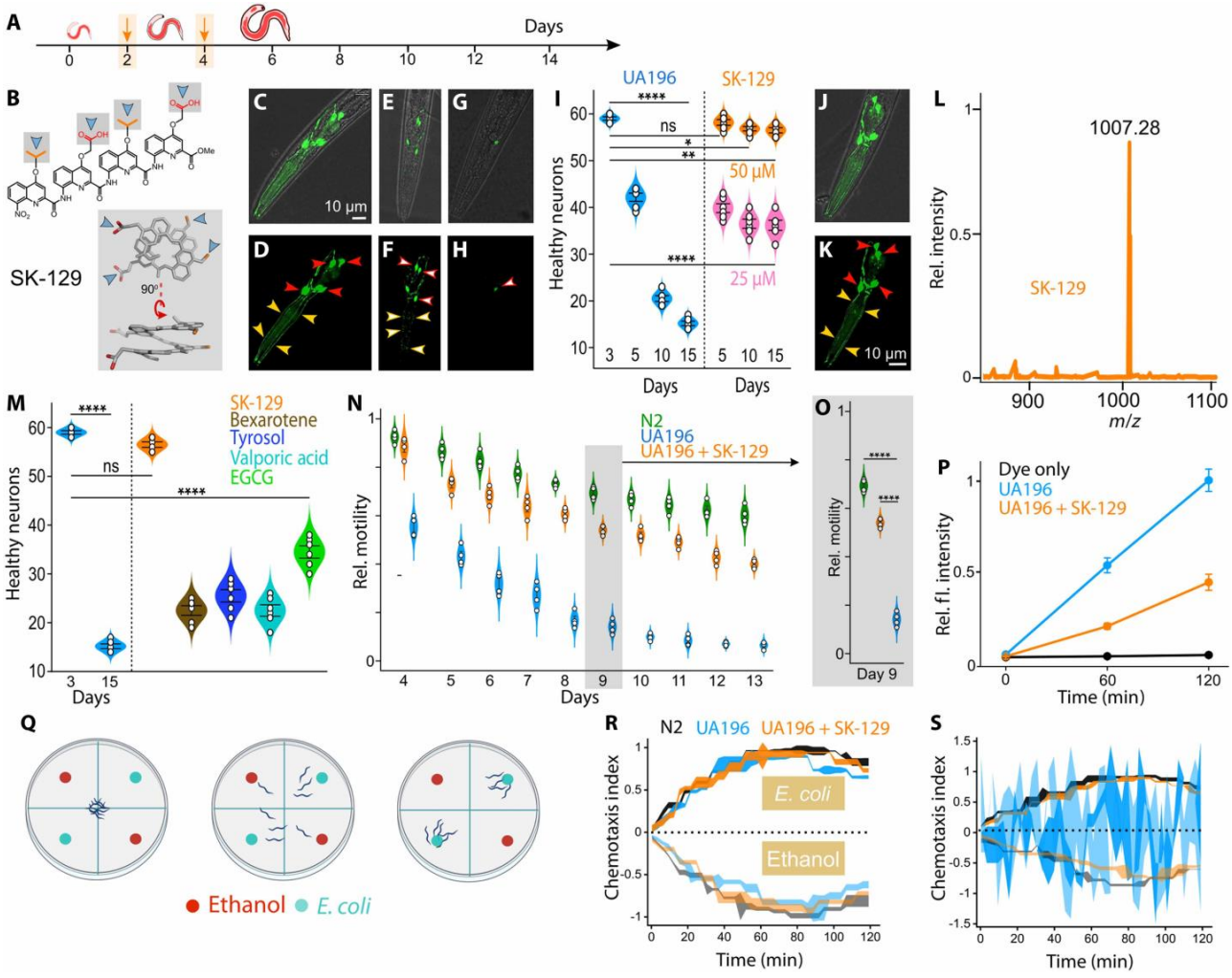

Fig. 1. SK-129 exhibits neuroprotective effects in *C. elegans* DA neurons. (**A**) Schematic for the treatment of UA196 worms with SK-129 on days 2 and 4 (arrows). (**B**) chemical and a crystal structure of SK-129 depicting side chains (blue arrows). (**C** to **H**) representative combined images (white field and confocal) of DA neurons in UA196 worms expressing αS and GFP on days 3 [(c) and (D)], 5 [(e) and (F)], and 15 [(G) and (h)]. Filled red and yellow arrows = healthy neurons and neurites, empty red and yellow arrows = degenerated neurons and neurites. (**I**) numbers of healthy neurons in UA196 worms (±SK-129 doses). (**J** and **K**) representative combined images of DA neurons in SK-129 treated UA196 worms (day 15). (**L**) hrMS of SK-129 from UA196 worms after 10 days. (**M**) numbers of healthy neurons in UA196 worms (±50 μM indicated ligands). (**N** and **O**) relative motility (normalized to n2) for 13 days of n2 and UA196 and statistics (for day 9, o) (±50 μM SK-129). (**P**) Quantification of the roS in UA196 worms on day 8 (±50 μM SK-129). (**Q**) Schematic of assay to assess the behavioral deficits in UA196 worms in the presence of ethanol and *E. coli*. (**R** and **S**) The ci graph for n2, UA196 worms (±50 μM SK-129) on day 3 (r) and day 10 (S). roS quantification for ≥50 worms per condition ($n = 3$; $N = 5$). confocal imaging analyzed ≥10 worms per experiment, with healthy neurons (YFP) manually quantified across $n = 6$ independent experiments; images are representative of 10 fields. Motility assays used 50 worms in duplicate ($n = 4$). chemotaxis assays used 50 worms per condition ($n = 3$; $N = 2$). Data are expressed as means ± SeM. *P* values were determined by one-way AnoVA with Tukey's multiple comparisons test where relevant. *$P < 0.05$, **$P < 0.01$, and ****$P < 0.0001$. *m/z*, mass/charge ratio; ns, nonsignificant.

The number of healthy DA neurons in untreated worms declined from 58.5 (day 3) to 41.5 (day 5), 21 (day 10), and 13.2 (day 15) (Fig. 2E). In contrast, treatment with SK-129 on day 5 resulted in 38.4 and 31.8 healthy DA neurons on day 15 at 50 and 25 μM, respectively, indicating robust, dose-dependent rescue (Fig. 2E). Other reported ligands showed minimal efficacy under matched conditions, yielding 13.3, 13.5, 13.3, and 21.5 healthy neurons for bexarotene, tyrosol, valproic acid, and EGCG, respectively (Fig. 2E). We next assessed motility after postdisease treatment (fig. S2A). The motility of untreated UA196 worms declined markedly with age relative to controls (fig. S2, B and C). In contrast, treatment with SK-129 (50 μM on day 5) improved the motility (fig. S2, B and C). We also evaluated ROS production in the postdisease model. ROS levels were measured on day 5, followed by treatment with SK-129 (50 μM), and reassessed on day 8 (Fig. 2F). The untreated UA196 worms showed elevated ROS because of αS aggregation and DA neuron degeneration (Fig. 2F) (*28*, *35*, *36*). In marked contrast, ROS levels were reduced in the presence of SK-129 (Fig. 2F). Together, these results demonstrate that SK-129 effectively rescued neurodegeneration, motor deficits, and oxidative stress in both early and postdisease PD models.

SK-129 inhibits intracellular αS aggregation in HEK cells

We tested the effect of SK-129 on intracellular aggregation of wild-type (WT) αS in human embryonic kidney (HEK) cells using a

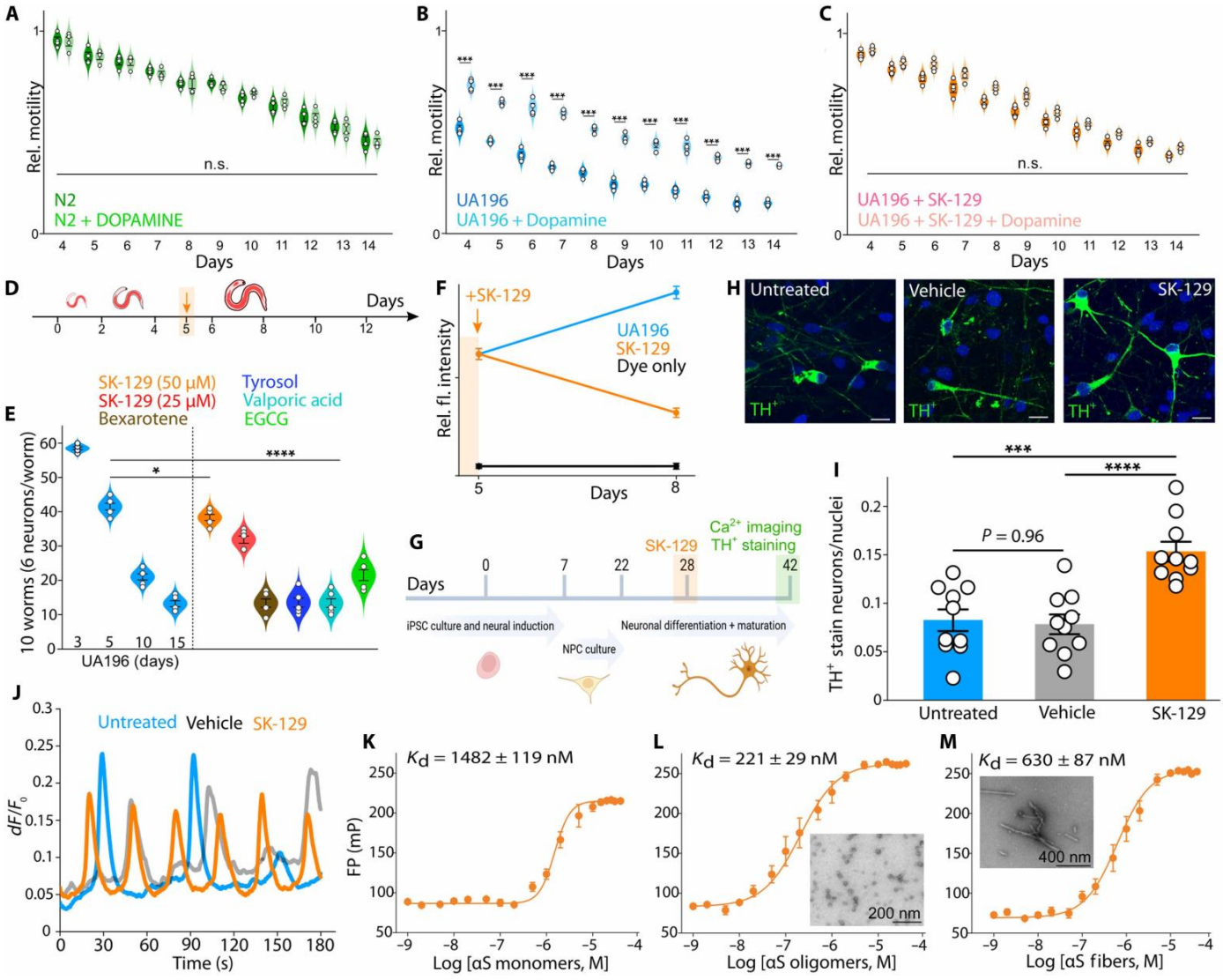

Fig. 2. SK-129 rescues PD phenotypes in *C. elegans* and iPSC-derived neurons. (**A** to **C**) Motility of n2 worms [±2 mM dopamine (A)], UA196 worms [±2 mM dopamine (B)], and UA196 worms+50 µM SK-129 [±2 mM dopamine (c)]. (**D**) Schematic of the treatment of UA196 worms with SK-129 (day 5). (**E**) numbers of healthy neurons in UA196 worms when treated on day 5 with the indicated ligands (50 µM). (**F**) Quantification of the roS on day 8 in UA196 worms (±50 µM SK-129, treatment day 5). (**G**) Timeline for treatment of iPSc-derived neurons with SK-129 (10 µM, every third day) and the testing of PD phenotypes. (**H** and **I**) confocal images [(h, 4′,6-diamidino-2-phenylindole (DAPi) and Th antibody–Alexa Fluor 488)] and quantification (i) of Th (green) in iPSc-derived neurons under the indicated conditions. (**J**) representative calcium traces of iPSc-derived neurons imaged under various conditions, including untreated (blue), vehicle (gray), and 10 µM SK-129 (orange). (**K** to **M**) FP titration curves and K_d values for the titration between $SK\text{-}129_F$ and αS monomer (K), αS oligomers (l), and αS fibers (M). Motility assays used 50 worms in duplicate per condition ($n = 4$ independent experiments; $N = 2$ technical replicates). roS quantification used ≥50 worms per condition ($n = 3$; $N = 2$). For confocal imaging, healthy neurons from 10 worms per ligand were manually counted per condition (day) across $n = 6$ independent experiments ($N = 2$). FP titrations were performed in triplicate using fresh stocks of αS conformers and $SK\text{-}129_F$; fit values represent the mean with SD. Data are expressed as means ± SeM. *P* values were determined by one-way AnoVA with Tukey's multiple comparisons test where relevant. $^*P < 0.05$, $^{**}P < 0.01$, $^{***}P < 0.001$, and $^{****}P < 0.0001$.

well-established model that stably expresses yellow fluorescent protein (YFP)–labeled WT αS (αS-YFP) in the cytoplasm (*23*, *24*, *44*). In this system, transfection with preformed αS fibers templates endogenous monomeric αS-YFP into intracellular aggregates using Lipofectamine 3000 (*23*, *24*, *44*).

Two conditions were used to evaluate inhibition and disaggregation of αS by SK-129. In the pre condition, HEK cells were treated with 10 µM SK-129 for 24 hours, followed by incubation with 1 µM preformed αS aggregates for 24 hours (fig. S3A). In the post condition, cells were first incubated with 1 µM preformed αS aggregates for 24 hours, followed by treatment with 10 µM SK-129 for 24 hours (fig. S3A).

The confocal microscopy revealed extensive intracellular αS-YFP puncta in cells treated with αS fibers (fig. S3B). In contrast, SK-129 treatment under both pre and post conditions markedly reduced puncta to levels comparable to controls (fig. S3B). These results were validated using a ProteoStat dye–based assay, which selectively stains amyloid aggregates (*24*, *28*). The ProteoStat fluorescence was increased ~7-fold

in αS fiber–treated cells but was reduced to ~1.4-fold and ~2-fold under pre and post SK-129 treatment, respectively (fig. S3C).

SK-129 had no significant effect on HEK cell viability (fig. S4). Together, these data demonstrate that SK-129 potently inhibited and disaggregated intracellular WT αS aggregates without inducing cytotoxicity in HEK cells.

SK-129 rescues PD phenotypes in iPSC-derived DA neurons

To examine the effect of SK-129 in a more physiologically relevant PD model, we used patient-derived induced pluripotent stem cell (iPSC) midbrain DA neurons containing an *SNCA* gene triplication. These neurons exhibit reduced dopamine levels and impaired calcium activity compared with isogenic controls (*45*). We therefore tested whether SK-129 treatment could rescue these phenotypes.

The DA neurons were treated with 10 μM SK-129 from day 28, every third day until day 42, corresponding to neuronal maturation (Fig. 2G). Using a fluorescently tagged SK-129 analog ($SK\text{-}129_F$), we confirmed intracellular uptake of SK-129, with robust localization in neuronal somas and processes after 2 days of treatment (fig. S5).

Dopamine production was assessed by quantifying tyrosine hydroxylase–positive (TH^+) DA neurons, because TH is the rate-limiting enzyme for dopamine synthesis. SK-129 treatment resulted in an approximately twofold increase in TH^+ DA neurons compared with untreated or vehicle-treated controls (Fig. 2, H and I). Neuronal activity was evaluated using the calcium indicator Calbryte (*46*), revealing an increase in Ca^{2+} spike frequency in SK-129–treated DA neurons relative to controls (Fig. 2J and fig. S6, A to C). Together, these results demonstrate that SK-129 rescued PD-associated deficits in dopamine production in iPSC-derived DA neurons.

SK-129 binds specifically to αS oligomers

We used fluorescence polarization (FP) titrations to quantify the binding affinity of SK-129 for different αS conformations, including monomers, oligomers, and fibers. The increasing concentrations of αS conformers were titrated into 100 nM $SK\text{-}129_F$ until FP signal saturation was reached (Fig. 2, K to M) and the fitting of the FP titration curves yielded dissociation constants (K_d) of 1482 ± 119, 221 ± 29, and 630 ± 87 nM for αS monomers (Fig. 2K), αS oligomers (Fig. 2L), and αS fibers (Fig. 2M), respectively. These data indicate that SK-129 bound αS oligomers and fibers with ~6-fold and ~3-fold higher affinity, respectively, than αS monomers. Thus, SK-129 preferentially interacted with pathological αS conformations.

SK-129 shows higher affinity for αS oligomers than other amyloid proteins

We compared the binding affinity of SK-129 for αS oligomers with its affinity for other amyloid proteins, including Aβ and tau, whose aggregation is associated with neurodegenerative disorders (*47*). The K_d of $SK\text{-}129_F$ for tau monomers, tau fibers, Aβ monomers, and Aβ fibers were 5.75 ± 0.85, 2.88 ± 0.61, 6.17 ± 0.98, and 3.09 ± 0.51 μM, respectively (fig. S7, A to D). Notably, SK-129 exhibited ≥10-fold higher binding affinity for αS oligomers than for any conformation of Aβ or tau, demonstrating high specificity for pathological αS species with minimal binding to other neurodegeneration-related proteins.

Tau aggregation in cellular models is unaffected by treatment with SK-129

We tested the specificity of SK-129 against intracellular tau aggregation using a HEK293 tau RD P301S fluorescence resonance energy transfer (FRET) biosensor model that stably expresses tau RD P301S–CFP and tau RD P301S–YFP in the cytoplasm (*48*). The treatment with preformed WT tau fibers induces intracellular aggregation of tau P301S protein in this model (*48*).

The HEK cells were treated with 1 μM preformed WT tau aggregates using Lipofectamine 3000 and incubated for 24 hours to induce tau aggregation (fig. S8A). The cells were then treated with SK-129 (10 μM) and incubated for an additional 24 hours. The confocal microscopy showed no difference in the numbers of intracellular tau P301S puncta in the absence or presence of SK-129 (fig. S8B).

Tau aggregation was further quantified using a ProteoStat dye–based assay as shown by us previously (*24*, *28*). The ProteoStat fluorescence was increased in cells treated with WT tau fibers compared with controls (fig. S8C), but no noticeable change was observed upon SK-129 treatment (fig. S8C). Therefore, SK-129 did not have any effect on tau aggregation.

SK-129 demonstrates target engagement in *C. elegans* models

We used extracellular vesicles (EVs) from PD worms to demonstrate target engagement of SK-129 against αS aggregation. Misfolded αS species, including oligomers and fibrils, are secreted via EVs and retain seeding competence, enabling prion-like propagation of LB-like inclusions (*2–4*, *49*, *50*), and αS-positive EVs have been detected in biofluids from patients with PD (*51*). In worms expressing human αS, αS has been detected in EV fractions, supporting a conserved EV-mediated pathway for αS transmission (*52*). We therefore used EVs from *C. elegans* PD models to assess target engagement by SK-129.

We used the NL5901 and UA196 PD models, in which SK-129 potently inhibits αS aggregation and PD phenotypes. Consistent with our previous findings in NL5901 worms (*24*), worms were treated with SK-129 (50 μM; days 2 and 4), and EVs were isolated from 10-day-old worms using established protocols (*53*). Confocal imaging revealed abundant αS-YFP aggregates in untreated NL5901 worms (Fig. 3, A and C), whereas SK-129 treatment markedly reduced αS-YFP aggregation (Fig. 3, B and C).

The EVs isolated from NL5901 worms (±50 μM SK-129; Fig. 3D) were characterized by transmission electron microscopy (TEM)/confocal imaging and dynamic light scattering, revealing vesicles with an average size of ~100 nm across control (N2) and NL5901 worms, regardless of treatment (Fig. 3, E to I). The confocal imaging demonstrated that EVs from NL5901 worms contained green fluorescent cargo, likely corresponding to αS-YFP (Fig. 3G). The Western blot analysis confirmed the presence of αS-YFP in NL5901-derived EVs (Fig. 3J), consistent with previous reports (*54*).

The αS aggregates were quantified using a FRET-based sandwich immunoassay (*52*, *55*). Compared with control worms, NL5901 worms exhibited an increase in FRET signal, indicative of elevated αS aggregation (Fig. 3K). In contrast, EVs from SK-129–treated NL5901 worms showed a substantial reduction in αS aggregates, approaching control levels (Fig. 3K).

To assess the competence of EV-associated αS species to cross the cell membrane, we evaluated EV uptake by HEK cells. Confocal microscopy and flow cytometry confirmed efficient internalization of NL5901-derived EVs, with detectable αS-YFP fluorescence in the cytosol within 12 hours of exposure (Fig. 3, L and M, and fig. S9). The untreated cells showed minimal signal, indicating EV-mediated delivery of αS cargo.

To further investigate the internalization of EVs extracted from N2 worms, EVs were isolated and stained with carboxyfluorescein

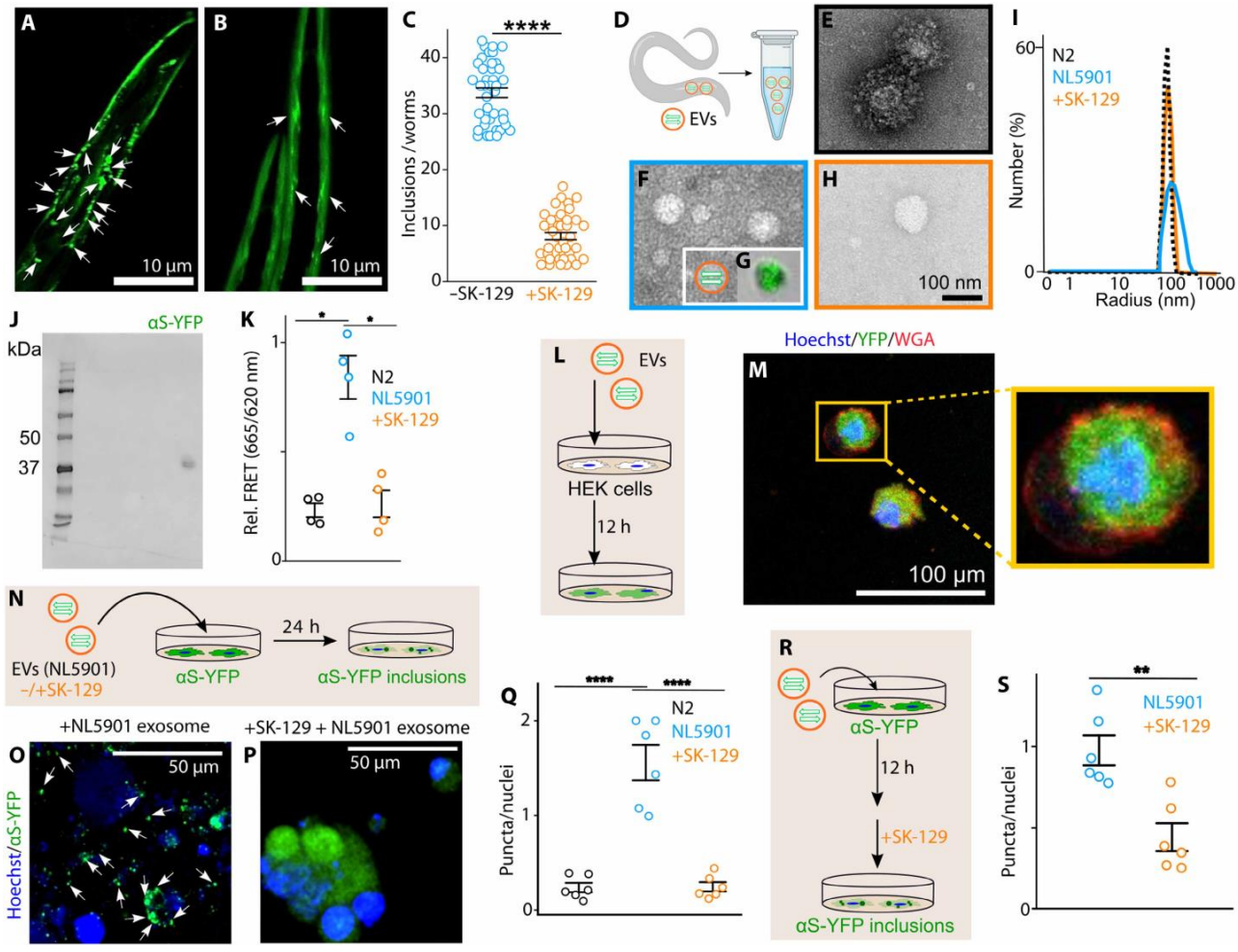

Fig. 3. Effect of SK-129 on the spread of αS aggregates from EVs derived from *C. elegans*. (**A** to **C**) representative confocal images [(A) and (B)] and quantification (c) of αS-YFP inclusions (white arrows) in muscle cells of nl5901 worms (day 10) in the absence (A) or presence (B) of 25 µM SK-129 (treated on days 2 and 4). (**D**) illustration of eV isolation from nl5901 worms. (**E** to **I**) representative TeM images [(e), (F), and (h)] and DIS analysis (i) of eVs from n2 (e), nl5901 (F), and nl5901 worms treated with 25 µM SK-129 (h) on day 10. (G) representative confocal image of nl5901 eVs. (**J**) Western blot analysis of eV lysates from nl5901 worms (day 10). (**K**) Quantification of αS aggregates in eV lysates from n2, nl5901, and nl5901 worms + 25 µM SK-129. (**L**) Schematic of eV transfer from nl5901 worms to heK cells. (**M**) representative confocal image of eV delivery of αS-A53T-YFP in heK cells (hoechst 33342 nuclear staining, wheat germ agglutinin membrane staining) treated for 12 hours with nl5901 eVs. (**N**) Schematic of eV transfer from nl5901 worms (±25 µM SK-129, days 2 and 4) to heK cells expressing αS-A53T-YFP. (**O** to **Q**) representative confocal images (hoechst 33342 nuclear staining) [(o) and (P)] and quantification of puncta (Q) in heK cells treated with eVs from nl5901 worms in the absence (o) or presence (P) of 25 µM SK-129. (**R**) Schematic of SK-129 treatment (25 µM) 12 hours after eV transfer from nl5901 worms (**S**). Quantification of puncta in heK cells treated with nl5901 eVs ± SK-129. For nl5901 confocal imaging, 10 worms per condition were analyzed across $n = 4$ independent experiments; inclusions were manually counted. eV isolation used ≥200 worms per condition across $n = 4$ independent experiments. heK cell assays were performed in $n = 4$ independent experiments; puncta/nuclei were manually counted, and flow cytometry used ≥10,000 cells per condition. Data are expressed as means ± SeM. *P* values were determined by one-way AnoVA with Tukey's multiple comparisons test where relevant. *$P < 0.05$, **$P < 0.01$, and ****$P < 0.0001$.

diacetate succinimidyl ester (CFSE) dye following a published procedure (*56*), which does not interfere with EV internalization. We treated HeLa cells with CFSE-stained EVs for 12 hours, and uptake was assessed by confocal microscopy and flow cytometry. Confocal imaging showed internalization of EVs in HeLa cells (fig. S10A). Consistently, fluorescence-activated cell sorting (FACS) analysis revealed a substantial population of CFSE-positive cells compared with control cells without EV exposure (fig. S10, B and C). These results confirm efficient cellular internalization of EVs derived from N2 worms.

Next, we tested the effect of SK-129 on intracellular aggregation of αS-A53T-YFP templated by αS aggregates present in EVs. We used a well-established HEK293T cell model that stably expresses monomeric YFP-labeled αS-A53T mutant in the cytosol (αS-A53T-YFP) (*23*, *24*, *28*, *44*). The endogenous αS-A53T-YFP can be templated into fibers upon exposure to preformed αS aggregates (*23*, *24*, *28*, *44*). The HEK cells expressing αS-A53T-YFP were treated with EVs isolated from NL5901 worms (±50 µM SK-129) for 24 hours, a time sufficient for EV internalization and aggregation templating (Fig. 3, N to Q).

The EVs from NL5901 worms induced αS-A53T-YFP puncta formation (Fig. 3, O and Q), whereas EVs from N2 worms did not (Fig. 3Q, black). Treatment with EVs from NL5901 worms (±50 µM

SK-129) resulted in a marked reduction in puncta (Fig. 3, P and Q), indicating efficient target engagement by SK-129.

Next, HEK cells were treated with EVs isolated from NL5901 worms on day 10, followed by addition of 10 μM SK-129 after 12 hours and incubation for an additional 24 hours (Fig. 3R). EV treatment resulted in ~1 puncta per nucleus (Fig. 3S, blue), whereas SK-129 substantially reduced puncta formation to ~0.4 puncta per nucleus (Fig. 3S, orange).

We further evaluated target engagement in UA196 worms, in which αS aggregation drives degeneration of DA neurons. EVs were extracted from UA196 worms (±50 μM SK-129) using the same protocol as for NL5901 worms. EV size was ~100 nm for control (N2) and UA196 worms (±SK-129; fig. S11A). The αS aggregate levels in EVs from UA196 worms were markedly higher than those from control worms and UA196 worms treated with SK-129 (fig. S11B). EVs from UA196 worms efficiently templated intracellular αS-A53T-YFP aggregation in HEK cells (~2 puncta per nucleus; fig. S11, C and E), whereas EVs from SK-129–treated UA196 worms resulted in a substantial decline in puncta (~1 puncta per nucleus; fig. S11, D and E). SK-129 also potently inhibited fiber-catalyzed αS-A53T-YFP aggregation when added 12 hours before or after EV treatment (<1 puncta per nucleus; fig. S11E, pre- and post-treated), with puncta numbers approaching control levels. Collectively, these results demonstrate robust target engagement by SK-129 in two *C. elegans* PD models and potent antagonism of EV-mediated, fiber-catalyzed intracellular αS aggregation.

We further tested the antagonist activity of SK-129 against fiber-catalyzed αS aggregation using neuron-derived exosomes (NDEs) isolated from patients with PD (Table 1). The blood samples from patients with PD and control individuals were used to isolate NDEs from plasma following published protocols (Fig. 4A) (*57*). The size of control and PD NDEs was ~100 nm, consistent with reported values (Fig. 4, B to D). Western blot analysis confirmed the presence of L1CAM, a neuronal transmembrane protein and established NDE marker, in both control and PD samples (fig. S12) (*57*). The quantification of αS aggregates using a FRET-based immunoassay revealed substantially higher levels of αS aggregates in PD-derived NDEs compared to controls (Fig. 4E). We next evaluated the ability of NDEs to template intracellular αS aggregation.

NDEs were stained with CFSE dye and incubated with HeLa cells for 12 hours. Confocal microscopy demonstrated efficient internalization of NDEs (fig. S10A), which was further confirmed by FACS analysis showing a substantial population of CFSE-positive cells compared with control cells without exosome exposure (fig. S10, B and C). To further confirm the internalization of preformed α-synuclein fibers (αS PFFs) and to distinguish templated intracellular aggregation of αS-A53T-YFP from spontaneous aggregation, we prepared Alexa633-labeled αS PFFs (αS-633 PFFs) using a reported protocol (*21*, *27*). HEK cells expressing cytosolic αS-A53T-YFP were treated with 1 μM αS-633 PFFs for 24 hours, washed with phosphate-buffered saline (PBS), and analyzed by live-cell confocal imaging (fig. S13A). Two types of puncta were detected. The first showed colocalization of internalized αS-633 PFFs (fig. S13A) with intracellular αS-A53T-YFP aggregates (fig. S13A, merge, yellow), demonstrating templated aggregation by internalized αS PFFs. The second type consisted of αS-A53T-YFP puncta lacking the Alexa 633 signal (fig. S13A, merge, green), consistent with spontaneous aggregation. The internalization of αS-633 PFFs was further confirmed by flow cytometry. Compared with control cells (fig. S13, B and C), a large population of cells exhibited the Alexa 633 signal after treatment with αS-633 PFFs (fig. S13, B and C, red), confirming efficient uptake and seeding of intracellular αS-A53T-YFP.

Table 1. Demographic information for control and PD cohorts to extract NDEs.

Age (year)	Gender	Disease duration (year)
	PD	
60.5	Male	1
51.3	Female	19
71.1	Male	9
67.5	Female	8
61	Female	not applicable (n/A)
67	Female	n/A
65	Male	n/A
64	Female	n/A
68	Female	n/A

To assess the ability of NDEs to template αS-A53T-YFP, HEK cells were treated with control or PD-derived NDEs for 24 hours (Fig. 4A). The control NDEs did not induce puncta formation (Fig. 4, F and H), whereas PD NDEs robustly templated αS-A53T- YFP into intracellular aggregates (Fig. 4, G and H). Adding 10 μM SK-129 12 hours before or after PD NDE treatment (Fig. 4, H to J, pre- and posttreated) markedly reduced puncta formation, indicat- ing potent inhibition of fiber-catalyzed αS aggregation.

SK-129 demonstrates favorable pharmaceutical properties in animal models

The pharmacokinetic properties of SK-129 were evaluated in vivo in mice. A single intravenous dose of SK-129 (20 mg/kg) was administered, and compound concentrations in plasma and brain homogenates were quantified over 0 to 72 hours by liquid chromatography tandem mass spectrometry (Fig. 5, A and B, and Table 2) (*26*, *30*, *58*–*60*). This dose enabled comparison with reported ligands for neurodegenerative disorders (*26*, *30*, *58*, *59*).

SK-129 exhibited an in vivo circulation half-life ($T_{1/2}$) of ~1.8 hours (Fig. 5A and Table 2), longer than that of αS-targeting small molecules such as minzasolmin ($T_{1/2}$ ~ 0.7 hour) (*26*). This extended circulation resulted in sustained brain accumulation over 72 hours, yielding a peak brain concentration (C_{max}) of 13.1 ± 0.3 μg/ml and a brain-to-plasma ratio of 9.4% (Fig. 5B and Table 2). The stability and unbound fraction of SK-129 were assessed in mouse plasma, brain homogenate, and human liver microsomes using established protocols (see Materials and Methods for details) (Fig. 5, C to E, and Table 3). SK-129 showed high stability in mouse plasma (91.9 ± 4.8%), brain homogenate (87.3 ± 3.2%), and human liver microsomes (94.5 ± 5.3%) (Fig. 5, C to E, and Table 3). The protein-unbound fraction was 4.4 ± 0.4, 29.9 ± 3.6, and 7.1 ± 0.8% in mouse plasma, brain homogenate, and human liver microsomes, respectively (Table 3). Overall, SK-129 demonstrated optimal pharmaceutical properties in mice (plasma and brain) and human liver microsomes.

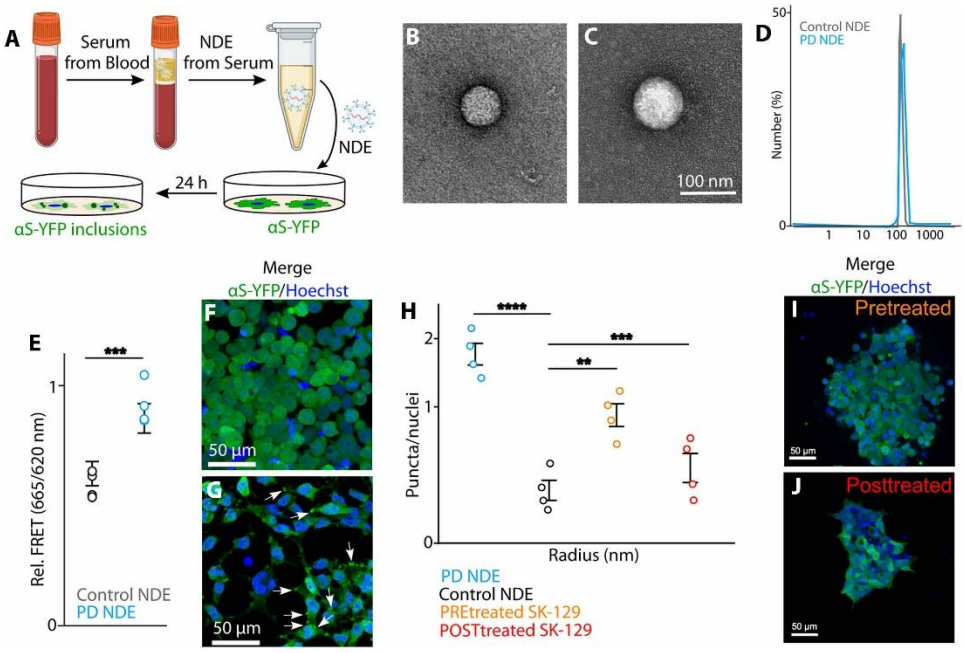

Fig. 4. Effect of SK-129 on the spread of αS aggregates from exosomes derived from patients with PD. (**A**) Schematic of nDe isolation from patient samples and transfer to heK cells. (**B** to **D**) representative TeM images [(B) and (c)] and DlS analysis (D) of nDes from a control (B) and a patient with PD (c). (**E**) Quantification of αS aggregates in pooled nDe lysates from control and PD samples. (**F** and **G**) representative confocal images of αS-YFP in heK cells (hoechst 33342 nuclear staining) treated for 24 hours with nDes from controls (F) or patients with PD (G); white arrows indicate puncta. Scale bars, 50 μm. (**H**) Quantification of αS puncta. (**I** and **J**) representative confocal images of heK (hoechst 33342 nuclear staining) cells pretreated with SK-129 (10 μM, 12 hours; i) or posttreated with SK-129 (10 μM, 12 hours; J), followed by exposure to control or PD nDes. heK cell experiments were performed across $n = 4$ independent experiments, with puncta/nuclei manually counted. Data are expressed as means ± SeM. *P* values were determined by one-way AnoVA with Tukey's multiple comparisons test where relevant. $^{**}P < 0.01$, $^{***}P < 0.001$, and $^{****}P < 0.0001$.

SK-129 inhibits spread of αS aggregates in PD mouse models

We next assessed SK-129's effect in the M83(A) mouse model. In this model, transgenic mice expressing mutant human A53T αS are injected with preformed αS aggregates, which accelerates PD phenotypes and reduces survival (median ~ 180 days) compared with untreated M83 mice (median ~ 360 days), likely through templating of intracellular A53T αS (*61*).

Eight-week-old M83 mice were stereotactically injected with αS aggregates (100 μM, 200 nl) derived from postmortem PD brain tissue into the substantia nigra (SN; anterior-posterior, −3.4; medial-lateral, ±1.4; dorsal-ventral, −4.0), following published protocols (Fig. 6A) (*62*). Two weeks later, mice were randomized to receive intravenous injections of either vehicle (saline + 2% dimethyl sulfoxide) or SK-129 (20 mg/kg) every other day for 21 days (10 doses; Fig. 6A). Alternate-day dosing was used because of the prolonged persistence of SK-129 in brain tissue (Fig. 5B and Table 2).

The body weight was monitored every 10 days until 270 days of age (Fig. 6B). As reported previously, vehicle-treated M83(A) mice exhibited weight loss (Fig. 6B) (*61*). In contrast, SK-129–treated M83(A) mice showed weight gain comparable to that of control mice (Fig. 6B). Median survival of vehicle-treated M83(A) mice was ~175 days, with fewer than 20% surviving to 270 days (Fig. 6, C and D), and surviving mice displayed severe motor deficits, including quadriparesis and postural abnormalities (Fig. 6D) (*61*, *62*). In contrast, SK-129–treated M83(A) mice exhibited 100% survival up to 270 days and showed no signs of motor impairment (Fig. 6, D and E). Immunohistochemical analysis was performed at 6 and 9 months to assess αS pathology across multiple brain regions (Fig. 6, F to O). Vehicle-treated M83(A) mice showed extensive deposition of phosphorylated αS (αS-129) and p62 throughout brain regions, whereas SK-129–treated mice showed no noticeable αS-129 or p62 aggregation at either time point (Fig. 6, F to M, and figs. S14 to S16). Microglial activation (Iba1 staining) was observed in vehicle-treated M83(A) mice but not in SK-129–treated mice (Fig. 6, N and O), consistent with reduced neuroinflammation (*63*). Also, the LB-associated biomarkers were quantified by counting stained regions within defined areas. Last, hematoxylin and eosin staining of major organs revealed no detectable abnormalities in SK-129–treated mice (fig. S17), indicating good tolerability and lack of systemic toxicity. Thus, the M83(A) model data confirmed that SK-129 is an effective and safe ligand for rescuing in vivo PD phenotypes.

Coaggregation of αS and tau is inhibited by SK-129

The coaggregation of αS and tau is a key pathological biomarker observed in PD and LBD (*8*–*10*). We therefore tested the antagonist activity of SK-129 against αS-tau coaggregation using a thioflavin T (ThT) aggregation assay. Both αS (1 mg/ml, 70 μM) and tau (1 mg/ml, 27.5 μM) were incubated in PBS with constant shaking at 37°C. Compared with αS alone (Fig. 7A), αS-tau coaggregation showed a shortened lag phase and a higher ThT signal (Fig. 7A), consistent with prior reports (*9*). Tau alone did not aggregate under these conditions (fig. S18). TEM imaging confirmed formation of αS-tau coaggregates, which were more compact and twisted than αS fibrils (Fig. 7, B and C). No detectable αS-tau coaggregation was observed in the presence of SK-129 at an equimolar concentration (70 μM), as validated by ThT and TEM (Fig. 7, A and D). In contrast, UCB0599, a clinical-stage PD ligand, failed to inhibit αS-tau coaggregation at an equimolar ratio (70 μM) (Fig. 7, A and E) (*54*). The cytotoxicity assessed by an MTT [3-(4,5-dimethylthiazol-2-yl)-2,5-diphenyltetrazolium bromide] assay showed that αS-tau coaggregates reduced cell viability to 12.2%, whereas SK-129 restored viability to 94.6% compared with 17.9% with UCB0599 (Fig. 7F). We further compared SK-129 with anle138b using the ThT assay where the ThT intensity of αS-tau coaggregation decreased from 100 to 1.4% with SK-129 but only to 77.8% with anle138b (fig. S19) (*64*). Similar trends were observed for αS aggregation alone, where SK-129 reduced ThT intensity to 1.8% compared with 72.2% with anle138b (fig. S20), demonstrating the superior antagonist activity of SK-129.

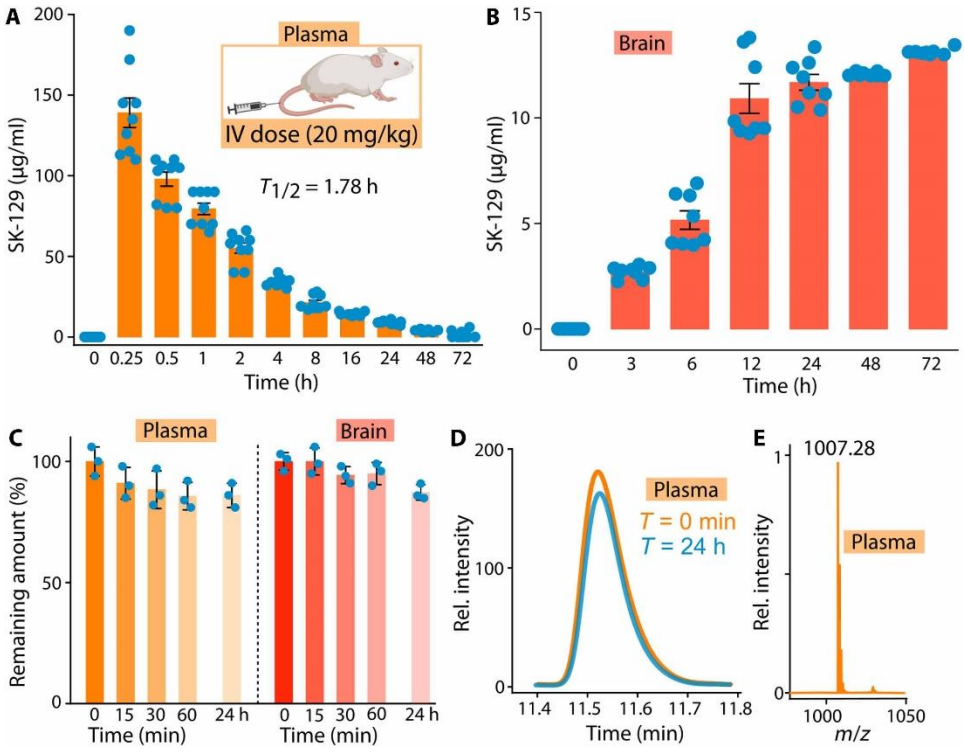

Fig. 5. Favorable in vivo pharmacokinetics of SK-129 in mice. (**A** and **B**) Plasma (A) and brain (B) concentrations of SK-129 after intravenous administration of SK-129 (20 mg/kg) in mice (n = 9 per group) at the indicated time points. (**C**) Time-dependent stability of SK-129 in mouse plasma and brain tissue. (**D**) representative hPlc traces of SK-129 (100 μM) after incubation with mouse plasma at the indicated time points and (**E**) representative hrMS after 24-hour incubation. All experiments were performed with n = 3 biological replicates. Data are presented as means ± SD.

Table 2. Physiochemical and in vivo pharmacological properties of SK-129. clogP, calculated partition coefficient (estimate of lipophilicity); tPSA, topological polar surface area.

Molecular weight	1006.28 g/mol
clogP	7.2
h- bond donors	5
h- bond acceptors	23
tPSA	306.3 Å^2
cell permeability	4.6 ± 0.1 × 10^{2}cm/s
C_{max} (blood plasma)	139.8 ± 26.7μg/ml
$T_{1/2}$ (blood plasma)	1.78 hours
C_{max} (plasma, 24 hours)	9 ± 1 μg/ml
C_{max} (brain)	13.1 ± 0.3 μg/ml
$T_{1/2}$ (brain)	>72 hours
ratio (brain/plasma)	9.4% (max)
C_{max} (brain, 72 hours)	13.1 ± 0.3 μg/ml

Table 3. Stability and fraction unbound of SK-129 under various in vivo conditions.

Mouse plasma stability (%, 24 hours)	91.9 ± 4.8
Mouse plasma unbound (%)	4.4 ± 0.4
Mouse brain stability (% 24 hours)	87.3 ± 3.2
Mouse brain unbound (%)	29.9 ± 3.6
human microsomal stability (% 24 hours)	94.5 ± 5.3
human microsomal unbound (%)	7.1 ± 0.8

We also examined the effect of SK-129 on preformed fiber-templated coaggregation of αS-tau. The preformed αS or αS-tau fibers accelerated αS aggregation (Fig. 7G), whereas no fiber formation was detected in the presence of SK-129 (70 μM) (Fig. 7G). Last, we evaluated whether inhibition of αS-tau coaggregation by SK-129 generated fiber-competent cytotoxic species using a cellular assay. The HEK293T cells expressing monomeric αS-A53T-YFP were transfected with preformed αS or αS-tau fibers (5 μM). The αS fibers induced puncta formation, whereas αS-tau fibers produced a higher number of smaller puncta, consistent with prior studies (*9*). In the presence of SK-129, puncta formation was markedly reduced (Fig. 7, H to J). The ProteoStat assay quantification confirmed these results, with fluorescence intensities reduced from 6.6- and 9.6-fold to 1.4- and 2.3-fold for αS (±SK-129) and αS-tau fibers (±SK-129), respectively (fig. S21).

SK-129 modulates condensates of αS-tau coaggregation

The previous studies have shown that tau complexes with αS to form liquid condensates by coacervation, which mature into aggregates of αS-tau (*9*, *11*, *65*). The condensates are nearly spherical (Fig. 7, K and L), whereas the puncta are irregular, nonspherical structures (Fig. 7, K and M), consistent with prior reports (*9*, *65*). We did not observe a noticeable number of puncta/condensates (P/C) when cells were treated with aggregated αS-tau solutions in the presence of SK-129 (Fig. 7, I and J, mixed).

We next tested whether SK-129 inhibits P/C formation templated by preformed αS or αS-tau fibers. HEK cells were pretreated with

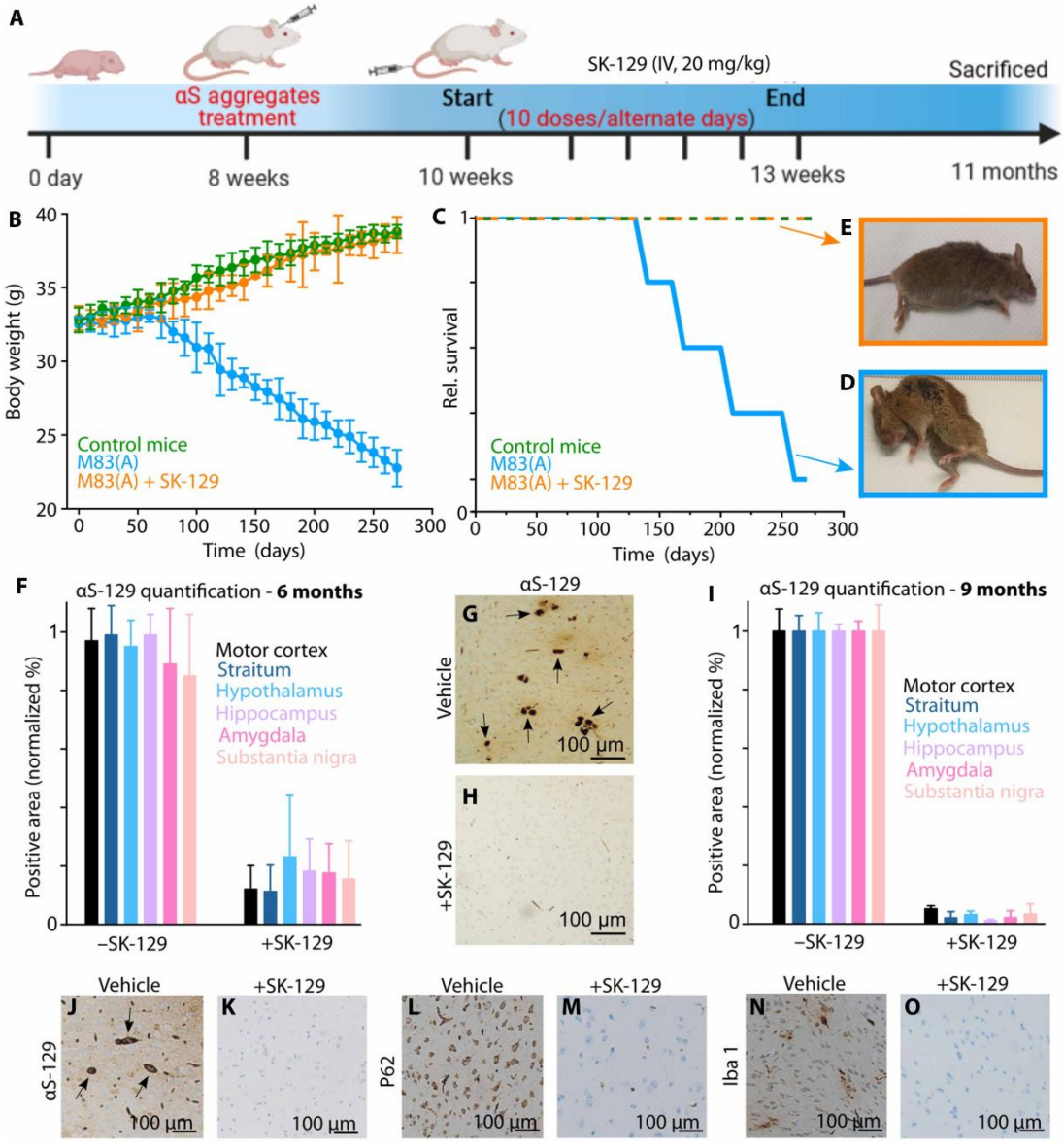

Fig. 6. SK-129 rescues PD phenotypes in a mouse model. (**A**) Schematic showing injection of preformed αS aggregates into Sn of M83 mice and intravenous administration of SK-129 (20 mg/kg) every other day from days 1 to 21 (n = 12 per condition; equal males and females; c57Bl as a control). (**B** to **E**) Body weights (B), survival (c), and representative images of M83 mice in the absence (D) or presence (e) of SK-129. (**F**) Quantification of pS129-αS in the Sn of M83 mice at 6 months. (**G** and **H**) representative ihc images in the absence (G) or presence (h) of SK-129. (**I**) Quantification of pS129-αS in the Sn at 9 months. (**J** to **M**) representative ihc images stained for pS129-αS and p62 in the absence [(J) and (l)] or presence [(K) and (M)] of SK-129. (**N** and **O**) representative iba1 staining of microglia in the absence (n) or presence (o) of SK-129. Scale bars, 100 μm. Data are presented as means ± SD (*n* = 3 to 10 mice).

10 μM SK-129 for 12 hours to allow internalization (*24*), followed by incubation with preformed αS or αS-tau fibers (5 μM) for 24 hours (fig. S22A). Compared with untreated cells (Fig. 7J and fig. S22B), preformed fibers induced a substantial increase in P/C formation (Fig. 7J and fig. S22C). In contrast, pretreatment by SK-129 markedly reduced P/C formation for both αS and αS-tau fibers (Fig. 7J, preaddition and fig. S22D). The ProteoStat assay quantification confirmed these results, with fluorescence intensities reduced from 6.6- and 9.6-fold to 1.5- and 2.5-fold for αS and αS-tau fibers, respectively, in the presence of SK-129 (fig. S23).

To study the effect of SK-129 on the condensates of αS-tau, we used a recently established experimental system that demonstrates the colocalization of αS-tau, the formation of condensates, and eventual termination into amyloids (*11*). Both αS (20 μM; 19 μM unlabeled +1 μM AF488 labeled) and tau (10 μM; 9 μM unlabeled +1 μM Atto647N labeled) were mixed [1× PBS (pH 7.4), 10% polyethylene glycol (PEG), and 0.02% NaN_3]. The addition of 1 μM $SK\text{-}129_F$ resulted in its colocalization and accumulation within αS-tau condensates (Fig. 7N and fig. S24), confirmed by fluorescence analysis (Fig. 7, O and P).

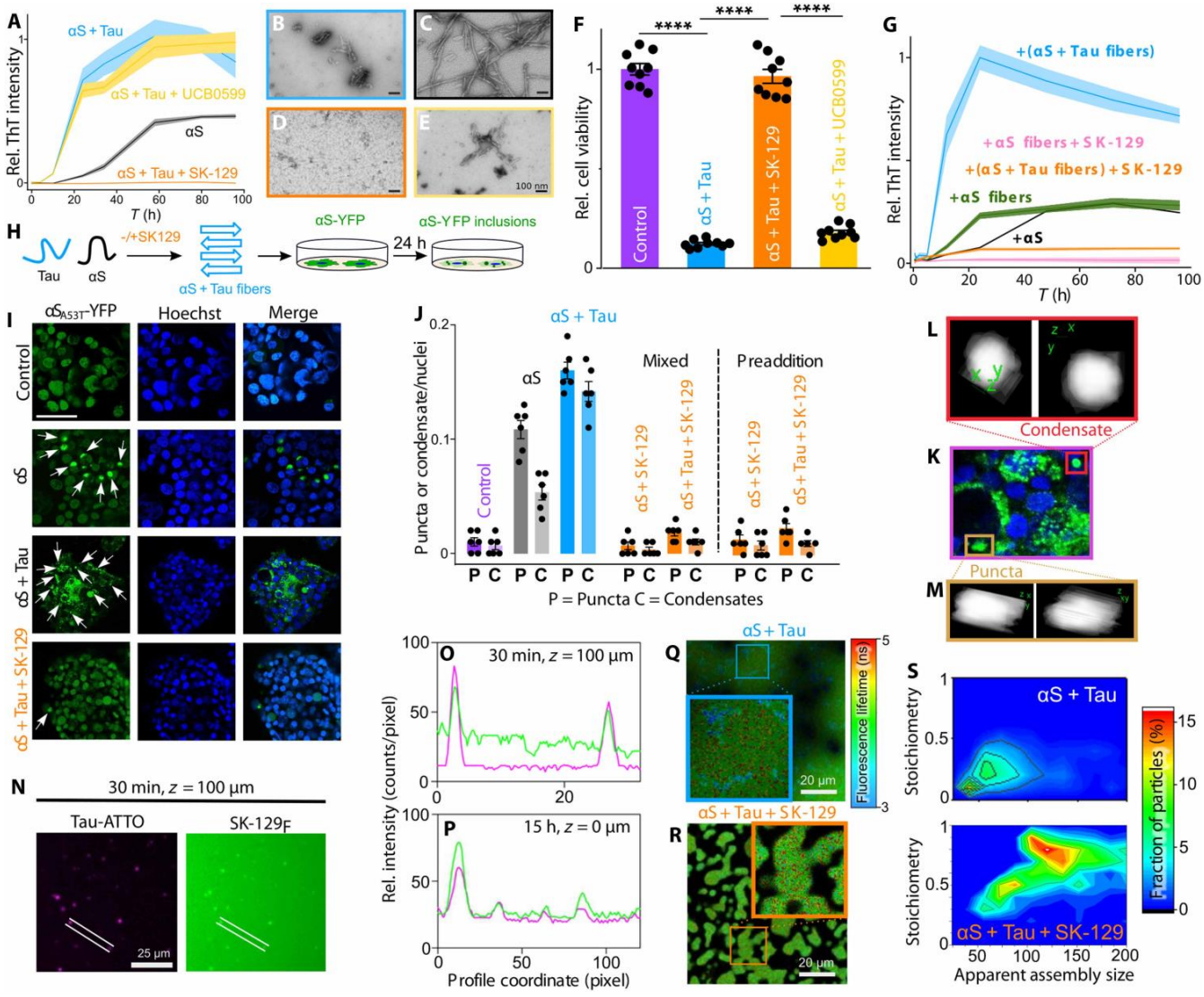

Fig. 7. SK-129 modulates the coaggregation of αS-tau. (**A**) Aggregation kinetics of αS (70 μM) and αS-tau (70/35 μM) in the absence or presence of ligands at equimolar ratios. (**B** to **E**) representative TeM images of end-point aggregates from αS-tau (B), αS (c), αS-tau + SK-129 (D), and αS-tau + UcB0599 (e) conditions. Scale bars, 100 nm. (**F**) Viability of heK cells treated for 48 hours with aggregation end points from (A). (**G**) Seeded aggregation of αS-tau (70/35 μM) catalyzed by αS or αS-tau fibers (2%, v/v) ± SK-129. (**H**) Schematic of αS-tau coaggregation and cellular effects. (**I**) representative confocal images of heK cells (expressing αS-A53T-YFP, hoechst 33342 nuclear staining) treated with aggregated αS or αS-tau (5 μM) ± SK-129; P/c, white arrows; hoechst, blue. Scale bars, 50 μm. (**J**) Quantification of puncta and condensates per nucleus for heK cells treated with αS or αS-tau fibers aggregated in the absence and presence of SK-129 (mixed) and SK-129–pretreated heK cells (preaddition). (**K** to **M**) Zoomed confocal images (merge αS-A53T-YFP, hoechst 33342 nuclear staining) of αS-tau–treated cells highlighting condensates (l) and puncta (M). (**N**) representative confocal images of colocalization of premixed αS-tau (αS, green; tau-Atto, red) with SK-129/SK-129F after 30 min. (**O** and **P**) Fluorescence intensity profiles quantified at 30 min (o) and 15 hours (P). (**Q** and **R**) τ_{647} FliM images of αS-tau condensates (αS, Atto647n-labeled tau) ± SK-129F after 15-hour incubation (25°c). (**S**) Single-molecule fluorescence analysis showing assembly stoichiometry versus apparent size of salt-resistant αS-tau assemblies ± SK-129. ThT data [(A) and (G)] are means ± SD ($n = 3$). cell viability (F) data are means ± SeM ($n = 4$ biological replicates, $N = 4$ technical replicates). confocal images are representative of 10 fields from $n = 4$ independent experiments. P/c were manually counted from ≥50 cells per condition (means ± SeM; $n = 4$ biological replicates, $N = 2$ technical replicates). Data are expressed as means ± SeM. *P* values were determined by one-way AnoVA with Tukey's multiple comparisons test where relevant. $^*P < 0.05$, $^{**}P < 0.01$, $^{***}P < 0.001$, and $^{****}P < 0.0001$.

We then followed the maturation of the αS-tau condensates in the presence of SK-129 by fluorescence lifetime imaging microscopy (FLIM). We previously showed that amyloid aggregation inside the condensates can be identified by means of a reduction of the fluorescence lifetime of the fluorophores attached to the proteins as a consequence of a pronounced fluorescence quenching in the protein solid state (*11*). Using FLIM, we demonstrated the formation of amyloid-like aggregates inside αS-tau liquid condensates in the absence (Fig. 7Q) but not in the presence (Fig. 7R) of SK-129. These smaller aggregates are resistant to high salt concentrations (unlike the liquid condensates) and are enriched in the tau protein, as indicated by single-molecule fluorescence burst analysis (Fig. 7S), in agreement with the higher propensity of the tau protein to aggregate. In line with these findings, when a well-established amyloid

aggregation deficient tau variant (referred as AggDef-tau) was used to generate the heterotypic condensates, no salt-resistant aggregates were detected upon the aging of the condensates (fig. S25, A and C). However, when SK-129 was present, the αS-tau condensates underwent a rapid and drastic change in their maturation process toward a gel-like state, preventing the transition into amyloid-like aggregates (SK-129; fig. S25, B and D). These gel-like condensates become resistant to high salt concentrations, and their fluorescence burst analysis reflects the size and the stoichiometry of the initially formed liquid condensates [with a stoichiometry of approximately 1:1 between tau and αS (+SK-129; Fig. 7S and fig. S26)], characteristics of gel-like electrostatic αS-tau coacervates (*11*). These findings suggest that SK-129 inhibited the formation of amyloid-like coaggregates of αS-tau and directed condensates to amyloid-incompetent gel-like assemblies.

Formation of αS-tau P/C is modulated by SK-129

The preformed P/C of αS and tau contribute to synucleinopathy spreading through seed-catalyzed (prion-like) mechanisms (*8*–*11*). We therefore tested whether SK-129 modulates the seeding activity of αS-tau P/C under biophysical and cellular conditions (Fig. 8A).

Both αS and tau (70 μM + 27.5 μM; 1 mg/ml) were coaggregated for 96 hours in PBS (1200 rpm, 37°C) and then incubated with SK-129 (70 μM) for 24 hours. The ThT signal was close to the control levels (+SK-129) indicating modulation of preformed αS-tau aggregates by SK-129 (post-mix; Fig. 8B). The comparable ThT signals in pre- and postmix conditions suggest that SK-129 both inhibits aggregation and remodels preformed αS-tau aggregates (Fig. 8B). Compared with untreated αS-tau fibers (Fig. 8C), SK-129–treated fibers showed altered morphology, appearing smaller and less twisted (Fig. 8D). We next assessed whether SK-129–treated αS or αS-tau fibers could template intracellular αS-A53T-YFP aggregation in HEK cells. Untreated αS or αS-tau fibers induced a progressive increase in P/C formation (Fig. 8E), whereas SK-129–treated fibers did not induce a large number of P/C (fiber treated; Fig. 8E). The ProteoStat assay quantification confirmed these results where the fluorescence intensity increased 7.1- and 10.1-fold with αS and αS-tau fibers, respectively, but was reduced to 2.8- and 2.2-fold in the presence of SK-129 (fig. S27). Together, these data show that SK-129 modulated preformed αS-tau P/C and suppresses their seeding competence.

The decrease in P/C observed with SK-129–treated preformed αS or αS-tau fibers likely results from fiber modulation or direct binding of SK-129, thereby reducing their seeding ability. To test this, we examined the effect of SK-129 on the seeding activity of preformed αS-tau fibers in HEK cells expressing αS-A53T-YFP. The cells were treated with preformed αS-tau fibers (5 μM) for 24 hours, followed by the addition of SK-129 (10 μM) for an additional 24 hours (Fig. 8F). A large number of P/C were observed in cells treated with αS-tau fibers alone (postaddition; Fig. 8E). In contrast, SK-129 treatment resulted in a substantial reduction in P/C comparable to control levels (postaddition; Fig. 8E). A similar reduction was observed for SK-129–treated αS fibers. The ProteoStat assay quantification confirmed these findings where the fluorescence intensity increased 7.1- and 10.1-fold with αS and αS-tau fibers, respectively, but decreased to 2.3- and 2.8-fold in the presence of SK-129 (fig. S28). The confocal microscopy also demonstrated that $SK\text{-}129_F$ (1 μM) colocalized with preformed αS-tau condensates composed of αS (20 μM) and tau (10 μM) [1× PBS (pH 7.4) and 10% PEG], indicating stable association (fig. S29, A and B). When SK-129 was added to preformed αS-tau condensates, amyloid-like coaggregates formed within 5 hours in the absence of SK-129 (Fig. 8, G and H), whereas SK-129 promoted formation of gel-like αStau structures (Fig. 8, G and I), which we previously showed to be noncytotoxic and nonseeding. Last, SN sections from 9-month-old M83(A) mice were analyzed for αS-tau coaggregates. The phosphorylated αS and tau coaggregates were detected in vehicle-treated mice (Fig. 8, J and L) but were completely absent in SK-129–treated mice (Fig. 8, K and L). Together, these results demonstrate that SK-129 potently inhibited both αS aggregation and αS-tau coaggregation in cellular and in vivo models.

DISCUSSION

Synucleinopathies comprise a spectrum of neurodegenerative disorders (PD, LBD, and MSA) for which no disease-modifying therapies currently exist, underscoring the urgent need for new therapeutic strategies (*10*, *66*, *67*). There are multiple facets of αS that are toxic, including de novo aggregation, prion-like spread of αS fibrils, and coaggregation with tau. Although numerous ligands inhibit αS aggregation and rescue disease phenotypes in experimental models (*5*, *6*, *21*–*30*, *68*), most have failed to advance to preclinical development because of poor pharmaceutical properties, limited BBB penetration, structural complexity, unclear modes of action, and disease heterogeneity.

Here, we identified SK-129 as a potent foldamer antagonist of αS aggregation that selectively binds to αS oligomers and fibrils with higher affinity than αS monomers, indicating preferential targeting of pathological conformations. Although binding to monomeric αS cannot be fully excluded, dosing near the K_d for αS oligomers will be optimized to minimize interference with physiological αS function. SK-129 rescued αS aggregation phenotypes in cellular systems, multiple *C. elegans* models, iPSC-derived neurons, and a PD mouse model.

Using EVs from *C. elegans* disease models, we demonstrated target engagement by SK-129. SK-129 also inhibited the spread of αS aggregates mediated by NDEs from patients with PD, supporting activity under clinically relevant conditions. SK-129 exhibited stability in mouse plasma, mouse brain, and human liver microsomes, as well as efficient BBB penetration and prolonged brain exposure—key requirements for central nervous system (CNS) therapeutics.

Although SK-129 exceeds conventional small-molecule thresholds for molecular weight and calculated lipophilicity, it belongs to the OQ foldamer class, whose folded architectures are not well captured by standard drug-likeness metrics. OQs adopt compact, helical conformations that shield polar surface area and generate amphiphilic architectures, improving apparent lipophilicity, cellular permeability, and BBB penetration (*24*, *31*, *32*, *60*). Supporting this, closely related foldamers exhibit large discrepancies between calculated and experimentally measured log*P* values (*32*). We therefore propose that the folded architecture of SK-129 contributes to its favorable CNS exposure and prolonged brain residence, enabling sustained target engagement. Notably, SK-129 persisted in brain tissue beyond 72 hours at concentrations >20-fold higher than those reported for other ligands (*26*, *30*, *58*, *59*), supporting prolonged antagonism of αS aggregation or LB formation. More than 98% of lead small molecules for CNS disorders fail to gain US Food and Drug Administration approval because of inadequate BBB penetration (*66*, *69*). In contrast, SK-129 efficiently crossed the BBB and exhibited favorable in vitro physicochemical properties (Table 2), exceeding those of many reported BBB-penetrant ligands (*26*, *30*, *58*, *59*). Further, for a large number of drugs for

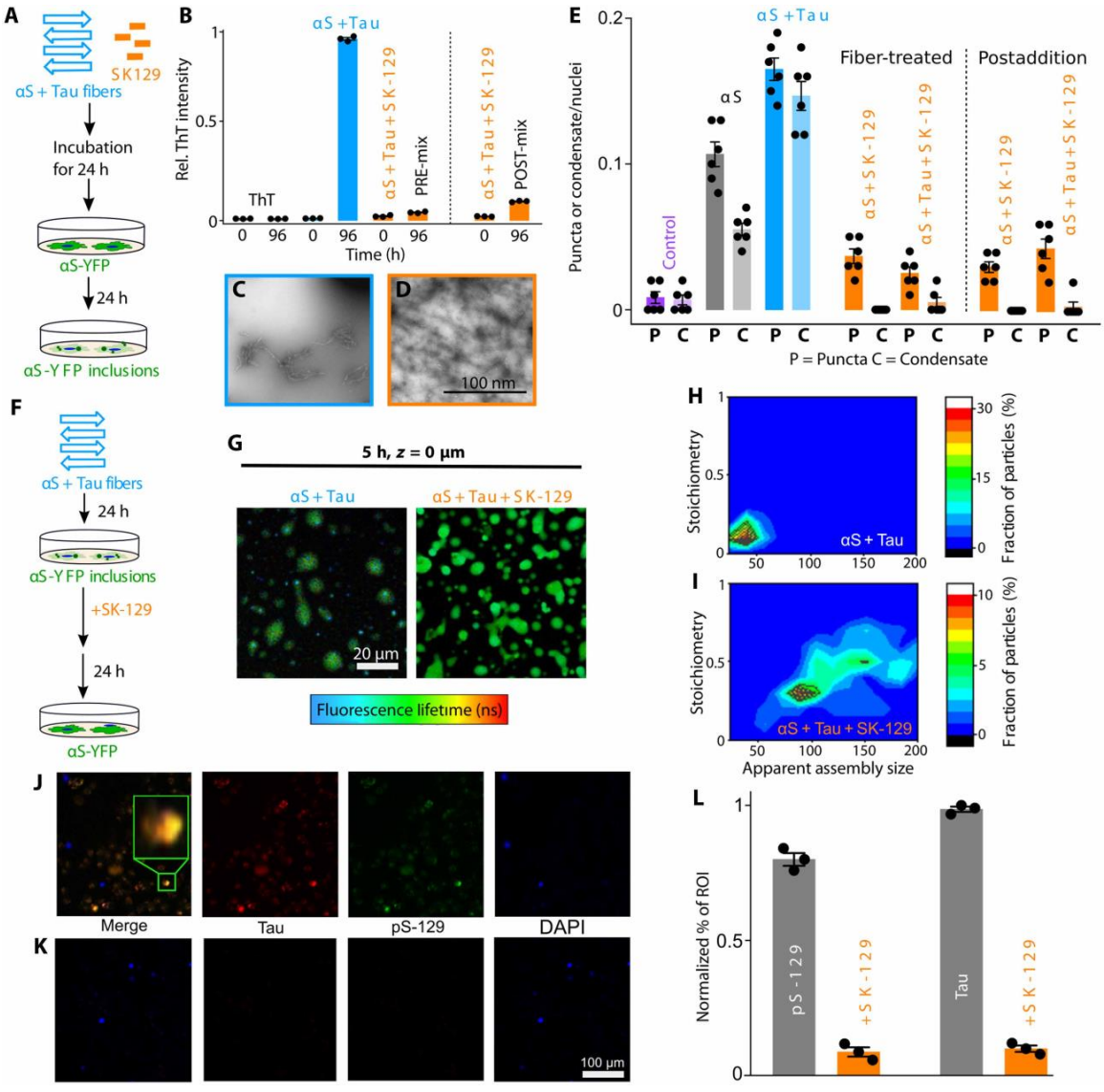

Fig. 8. SK-129 modulates the coaggregation of αS-tau in a postdisease model. (**A**) Schematic of SK-129 treatment of preformed αS-tau fibers and subsequent effects in heK cells. (**B**) ThT fluorescence of αS-tau aggregation or preformed αS-tau fibers (70/35 µM) treated with SK-129 (70 µM) at initiation or after fibril formation (0 and 96 hours). (**C**) representative TeM images of preformed αS-tau fibers. (**D**) representative TeM images after SK-129 treatment for 24 hours. (**E**) Quantification of puncta and condensates per nucleus in heK cells treated with SK-129–exposed preformed αS or αS-tau fibers (5 µM, fiber-treated) and after posttreatment with SK-129 (10 µM, postaddition). (**F**) Schematic of heK cell pretreatment with preformed αS or αS-tau fibers followed by SK-129 treatment. (**G**) FliM analysis of αS-tau condensates ± SK-129. (**H**) Single-molecule fluorescence analysis showing stoichiometry versus apparent aggregate size of salt-resistant αS-tau assemblies without SK-129 after nacl addition (500 mM). (**I**) Single-molecule fluorescence analysis of αS-tau assemblies in the presence of SK-129. (**J**) representative confocal images of Sn from 9-month-old M83 mice stained with DAPi, pS129-αS, AT8 (phosphorylated tau) and merged channels in the absence of SK-129. (**K**) representative confocal images in the presence of SK-129 (20 mg/kg, intravenous). (**L**) Quantification of pathology. ThT data (B) are means ± SD (n = 3). confocal images [(J) and (K)] are representative of 10 fields from n = 4 independent experiments. P/c (e) were manually counted from ≥50 cells per condition (means ± SeM; n = 4 biological replicates, N = 2 technical replicates).

neurodegenerative diseases, the fraction of unbound drugs is >1% (*69*). In comparison, SK-129 had a much higher fraction (>4%) unbound in all tested conditions (Table 3). Ongoing studies aim to further define the relationship between folding, unbound exposure, and brain distribution.

SK-129 was also a potent antagonist of αS-tau coaggregation, a pathological feature of PD and LBD that contributes to disease heterogeneity (*8*–*14*). The pathological αS species interact and accelerate tau misfolding and fibrillization. The preferential binding of SK-129 to αS oligomers and fibrils supports a mechanism in which SK-129 blocks αS-tau interactions and inhibits coaggregation. Together, the selective targeting of αS oligomers can inhibit αS aggregation, prion-like spread, and αS-tau coaggregation, addressing multiple pathogenic pathways underlying synucleinopathic heterogeneity. Overall, foldamers provide a synthetically tunable scaffold enabling concurrent optimization of efficacy and pharmaceutical properties, facilitating advancement toward clinical development for synucleinopathies.

Several limitations of our study should be acknowledged. First, the preferential binding of SK-129 to toxic αS oligomers over αS

monomers (~6-fold higher) and ~10-fold selectivity over other amyloid conformations was established primarily using in vitro assays. Whether this level of conformational specificity is maintained in vivo, particularly within the complex protein-rich environment of the brain, remains to be determined and may influence both therapeutic efficacy and off-target interactions. Second, although SK-129 did not exhibit apparent toxicity in mice, a comprehensive toxicological assessment including chronic dosing, dose-escalation, and organ-specific safety studies was not performed and will be necessary to rigorously define its therapeutic window. Third, neurodegeneration in UA196 worms is accompanied by dopamine depletion and reduced locomotor capacity, which may confound behavioral assays that depend on worms' active movement. Because SK-129 inhibits αS aggregation and prevents dopaminergic neuronal loss, treatment restores motility and neuronal circuit function. As a result, the apparent rescue of chemotaxis behavior may overestimate the extent of chemotactic sensory recovery and instead reflect, at least in part, improved motor output. Accordingly, chemotaxis assay data are interpreted here as an integrated sensorimotor readout of dopaminergic neuronal integrity rather than a measure of sensory processing alone. Future studies incorporating independent locomotor controls or motor-independent chemotaxis paradigms will be required to further dissociate motor and sensory contributions to behavioral rescue. Last, although SK-129 robustly rescued molecular and pathological hallmarks of synucleinopathy in vivo, behavioral outcomes were not assessed in the treated PD mouse model. It remains possible that pathological rescue may not fully translate into functional or behavioral improvement. Addressing these limitations through expanded in vivo specificity, safety, and behavioral efficacy studies will be critical to further validate the translational potential of SK-129 as a disease-modifying therapeutic for synucleinopathies. In summary, SK-129 emerges as a promising lead for disease-modifying intervention across synucleinopathies and provides strong mechanistic validation of αS oligomers and αS-tau coaggregation as therapeutic targets.

MATERIALS AND METHODS

Study design

The objective of this study was to evaluate a foldamer, SK-129, that inhibits α-synuclein aggregation as a disease-modifying therapeutic strategy for synucleinopathies. SK-129 was administered across biophysical, cellular, *C. elegans*, human iPSC-derived neuron, and mouse models, with efficacy assessed using aggregation and binding assays, cellular pathology and toxicity measurements, neurodegeneration readouts, pharmacokinetic and BBB penetration analyses, and histopathological evaluations. These complementary approaches demonstrated SK-129's ability in target engagement (αS oligomers/fibers), aggregation inhibition, neuronal protection, pathological rescue, and in vivo safety. Biophysical, cellular, *C. elegans*, and iPSC-based experiments were performed independently repeated at least three times; exact sample sizes are reported in the corresponding figure legends. Data collection for biophysical, cellular, and *C. elegans* experiments was terminated upon completion of prespecified experimental end points established in prior studies from our laboratory. Animals were randomly allocated to experimental groups, and all animals were included in the analyses. For mouse studies, experiments were terminated when disease progression in the PD model resulted in mortality exceeding 80% of animals in the affected group. No data points were excluded from any experiment. Investigators were blinded for at least one trial in biophysical, cellular, iPSC, and *C. elegans* experiments, during which the identity of experimental conditions was concealed from the investigator performing the assays. All mouse studies were conducted in accordance with ARRIVE (Animal Research: Reporting of In Vivo Experiments) Guidelines 2.0 and were approved by the Institutional Animal Care and Use Committees of New York University Abu Dhabi (approval no. 23-0003) and the University of Denver (approval no. 1635903-6). All human specimens were collected with informed consent under Institutional Review Board–approved protocols. Statistical methods were not used to predetermine sample size; however, sample sizes were consistent with common practice in the field.

Statistical analysis

Statistical analysis was carried out using GraphPad Prism or OriginLab OriginPro. Data are represented as the means ± SD or SEM as indicated throughout the manuscript. For comparisons involving more than two groups, ordinary one-way or two-way analysis of variance (ANOVA) was used with Tukey's multiple comparisons test where relevant. A P value of <0.05 was considered statistically significant throughout where $*P < 0.05$, $**P < 0.01$, $***P < 0.001$, and $****P < 0.0001$. All individual-level data are available in data file S1. For detailed methods, see the Supplementary Materials.

Supplementary Materials

The PDF file includes:
Materials and Methods
Figs. S1 to S29
references (*70–88*)

Other Supplementary Material for this manuscript includes the following:
Data files S1 and S2

REFERENCES AND NOTES

1. M. G. Spillantini, M. l. Schmidt, V. M.-Y. lee, J. Q. Trojanowski, r. Jakes, M. Goedert, α-synuclein in lewy bodies. *Nature* **388**, 839–840 (1997).
2. T. M. Dawson, V. l. Dawson, Molecular pathways of neurodegeneration in Parkinson's disease. *Science* **302**, 819–822 (2003).
3. M. Goedert, Alpha-synuclein and neurodegenerative diseases. *Nat. Rev. Neurosci.* **2**, 492–501 (2001).
4. P. calabresi, A. Mechelli, G. natale, l. Volpicelli-Daley, G. Di lazzaro, V. Ghiglieri, Alpha-synuclein in Parkinson's disease and other synucleinopathies: From overt neurodegeneration back to early synaptic dysfunction. *Cell Death Dis.* **14**, 1–16 (2023).
5. A. heras-Garvin, D. Weckbecker, S. ryazanov, A. leonov, c. Griesinger, A. Giese, G.K. Wenning, n. Stefanova, Anle138b modulates α-synuclein oligomerization and prevents motor decline and neurodegeneration in a mouse model of multiple system atrophy. *Mov. Disord.* **34**, 255–263 (2019).
6. r. Staats, T. c. T. Michaels, P. Flagmeier, S. chia, r. i. horne, J. habchi, S. linse, T.P. J. Knowles, c. M. Dobson, M. Vendruscolo, Screening of small molecules using the inhibition of oligomer formation in α-synuclein aggregation as a selection parameter. *Commun. Chem.* **3**, 1–9 (2020).
7. J. Burré, M. Sharma, T. c. Südhof, cell biology and pathophysiology of α-synuclein. *Cold Spring Harb. Perspect. Med.* **8**, a024091 (2018).
8. U. Sengupta, r. Kayed, Amyloid β, Tau, and α-Synuclein aggregates in the pathogenesis, prognosis, and therapeutics for neurodegenerative diseases. *Prog. Neurobiol.* **214**, 102270 (2022).
9. l. Pan, c. li, l. Meng, Y. Tian, M. he, X. Yuan, G. Zhang, Z. Zhang, J. Xiong, G. chen, Z.Zhang, Tau accelerates α-synuclein aggregation and spreading in Parkinson's disease. *Brain* **145**, 3454–3471 (2022).
10. W. li, J.-Y. li, overlaps and divergences between tauopathies and synucleinopathies: A duet of neurodegeneration. *Transl. Neurodegener.* **13**, 16 (2024).
11. P. Gracia, D. Polanco, J. Tarancón-Díez, i. Serra, M. Bracci, J. oroz, D. V. laurents, i. García, n. cremades, Molecular mechanism for the synchronized electrostatic coacervation and co-aggregation of alpha-synuclein and tau. *Nat. Commun.* **13**, 4586 (2022).

12. K. Arima, S. hirai, n. Sunohara, K. Aoto, Y. izumiyama, K. Uéda, K. ikeda, M. Kawai, cellular co-localization of phosphorylated tau- and nAcP/α-synuclein-epitopes in lewy bodies in sporadic Parkinson's disease and in dementia with lewy bodies. *Brain Res.* **843**, 53–61 (1999).
13. B. i. Giasson, M. S. Forman, M. higuchi, l. i. Golbe, c. l. Graves, P. T. Kotzbauer, J.Q. Trojanowski, V. M.-Y. lee, initiation and synergistic fibrillization of tau and alpha-synuclein. *Science* **300**, 636–640 (2003).
14. J. l. Guo, D. J. covell, J. P. Daniels, M. iba, A. Stieber, B. Zhang, D. M. riddle, l. K. Kwong, Y.Xu, J. Q. Trojanowski, V. M. Y. lee, Distinct α-synuclein strains differentially promote tau inclusions in neurons. *Cell* **154**, 103–117 (2013).
15. A. Bejanin, D. r. Schonhaut, r. la Joie, J. h. Kramer, S. l. Baker, n. Sosa, n. Ayakta, A.cantwell, M. Janabi, M. lauriola, J. P. o'neil, M. l. Gorno-Tempini, Z. A. Miller, h. J. rosen, B. l. Miller, W. J. Jagust, G. D. rabinovici, Tau pathology and neurodegeneration contribute to cognitive impairment in Alzheimer's disease. *Brain* **140**, 3286–3300 (2017).
16. M. A. G. Gilbert, n. Fatima, J. Jenkins, T. J. o'Sullivan, A. Schertel, Y. halfon, M. Wilkinson, T.h. J. Morrema, M. Geibel, r. J. read, n. A. ranson, S. e. radford, J. J. M. hoozemans, r. A. W. Frank, cryoeT of β-amyloid and tau within postmortem Alzheimer's disease brain. *Nature* **631**, 913–919 (2024).
17. r. J. Bateman, K. horie, o. hansson, A fluid biomarker accurately detects tau aggregate pathology in Alzheimer's disease. *Nat. Med.* **29**, 1912–1913 (2023).
18. K. horie, n. r. Barthélemy, c. Sato, r. J. Bateman, cSF tau microtubule binding region identifies tau tangle and clinical stages of Alzheimer's disease. *Brain* **144**, 515–527 (2021).
19. S. Dhakal, M. Mondal, A. Mirzazadeh, S. Banerjee, A. Ghosh, V. rangachari, α-Synuclein emulsifies TDP-43 prion-like domain—rnA liquid droplets to promote heterotypic amyloid fibrils. *Commun. Biol.* **6**, 1227 (2023).
20. D. M. Vadukul, M. Papp, r. J. Thrush, J. Wang, Y. Jin, P. Arosio, F. A. Aprile, α-synuclein aggregation is triggered by oligomeric amyloid-β 42 via heterogeneous primary nucleation. *J. Am. Chem. Soc.* **145**, 18276–18285 (2023).
21. J. Pujols, S. Peña-Díaz, D. F. lázaro, F. Peccati, F. Pinheiro, D. González, A. carija, S. navarro, M. conde-Giménez, J. García, S. Guardiola, e. Giralt, X. Salvatella, J. Sancho, M. Sodupe, T.F. outeiro, e. Dalfó, S. Ventura, Small molecule inhibits α-synuclein aggregation, disrupts amyloid fibrils, and prevents degeneration of dopaminergic neurons. *Proc. Natl. Acad. Sci. U.S.A.* **115**, 10481–10486 (2018).
22. M. Perni, c. Galvagnion, A. Maltsev, G. Meisl, M. B. D. Müller, P. K. challa, J. B. Kirkegaard, P.Flagmeier, S. i. A. cohen, r. cascella, S. W. chen, r. limbocker, P. Sormanni, G. T. heller, F.A. Aprile, n. cremades, c. cecchi, F. chiti, e. A. A. nollen, T. P. J. Knowles, M. Vendruscolo, A.Bax, M. Zasloff, c. M. Dobson, A natural product inhibits the initiation of α-synuclein aggregation and suppresses its toxicity. *Proc. Natl. Acad. Sci. U.S.A.* **114**, e1009–e1017 (2017).
23. S. Sangwan, S. Sahay, K. A. Murray, S. Morgan, e. l. Guenther, l. Jiang, c. K. Williams, h. V. Vinters, M. Goedert, D. S. eisenberg, inhibition of synucleinopathic seeding by rationally designed inhibitors. *eLife* **9**, e46775 (2020).
24. J. Ahmed, T. c. Fitch, c. M. Donnelly, J. A. Joseph, T. D. Ball, M. M. Bassil, A. Son, c. Zhang, A.ledreux, S. horowitz, Y. Qin, D. Paredes, S. Kumar, Foldamers reveal and validate therapeutic targets associated with toxic α-synuclein self-assembly. *Nat. Commun.* **13**, 2273 (2022).
25. J. Santos, P. Gracia, S. navarro, S. Peña-Díaz, J. Pujols, n. cremades, i. Pallarès, S. Ventura, α-helical peptidic scaffolds to target α-synuclein toxic species with nanomolar affinity. *Nat. Commun.* **12**, 3752 (2021).
26. D. l. Price, A. Khan, r. Angers, A. cardenas, M. K. Prato, M. Bani, D. W. Bonhaus, M. citron, A.-l. Biere, in vivo effects of the alpha-synuclein misfolding inhibitor minzasolmin supports clinical development in Parkinson's disease. *NPJ Parkinsons Dis.* **9**, 114 (2023).
27. G. Pagano, K. i. Taylor, J. Anzures cabrera, T. Simuni, K. Marek, r. B. Postuma, n. Pavese, F.Stocchi, K. Brockmann, h. Svoboda, D. Trundell, A. Monnet, r. Doody, P. Fontoura, G.A. Kerchner, P. Brundin, T. nikolcheva, A. Bonni, Prasinezumab slows motor progression in rapidly progressing early-stage Parkinson's disease. *Nat. Med.* **30**, 1096–1103 (2024).
28. n. h. Stillman, J. A. Joseph, J. Ahmed, c. Z. Baysah, r. A. Dohoney, T. D. Ball, A. G. Thomas, T.c. Fitch, c. M. Donnelly, S. Kumar, Protein mimetic 2D FAST rescues alpha synuclein aggregation mediated early and post disease Parkinson's phenotypes. *Nat. Commun.* **15**, 3658 (2024).
29. J. Pujols, S. Peña-Díaz, i. Pallarès, S. Ventura, chemical chaperones as novel drugs for Parkinson's disease. *Trends Mol. Med.* **26**, 408–421 (2020).
30. W. Wrasidlo, i. F. Tsigelny, D. l. Price, G. Dutta, e. rockenstein, T. c. Schwarz, K. ledolter, D.Bonhaus, A. Paulino, S. eleuteri, Å. A. Skjevik, V. l. Kouznetsova, B. Spencer, P. Desplats, T.Gonzalez-ruelas, M. Trejo-Morales, c. r. overk, S. Winter, c. Zhu, M.-F. chesselet, D.Meier, h. Moessler, r. Konrat, e. Masliah, A de novo compound targeting α-synuclein improves deficits in models of Parkinson's disease. *Brain* **139**, 3217–3236 (2016).
31. S. Kumar, A. henning-Knechtel, i. chehade, M. Magzoub, A. D. hamilton, Foldamer-mediated structural rearrangement attenuates Aβ oligomerization and cytotoxicity. *J.Am. Chem. Soc.* **139**, 17098–17108 (2017).
32. S. Kumar, M. Birol, D. e. Schlamadinger, S. P. Wojcik, e. rhoades, A. D. Miranker, Foldamer-mediated manipulation of a pre-amyloid toxin. *Nat. Commun.* **7**, 11412 (2016).
33. S.Dengler, r. T. howard, V. Morozov, c. Tsiamantas, W.-e. huang, Z. liu, c. Dobrzanski, V.Pophristic, S. Brameyer, c. Douat, h. Suga, i. huc, Display selection of a hybrid foldamer–peptide macrocycle. *Angew. Chem. Int. Ed.* **62**, e202308408 (2023).
34. A.ray, B. A. Martinez, l. A. Berkowitz, G. A. caldwell, K. A. caldwell, Mitochondrial dysfunction, oxidative stress, and neurodegeneration elicited by a bacterial metabolite in a *C. elegans* Parkinson's model. *Cell Death Dis.* **5**, e984 (2014).
35. S.Wang, S. Zhang, l.-c. liou, Q. ren, Z. Zhang, G. A. caldwell, K. A. caldwell, S. n. Witt, Phosphatidylethanolamine deficiency disrupts α-synuclein homeostasis in yeast and worm models of Parkinson disease. *Proc. Natl. Acad. Sci. U.S.A.* **111**, e3976–e3985 (2014).
36. D.e. Mor, S. Sohrabi, r. Kaletsky, W. Keyes, A. Tartici, V. Kalia, G. W. Miller, c. T. Murphy, Metformin rescues Parkinson's disease phenotypes caused by hyperactive mitochondria. *Proc. Natl. Acad. Sci. U.S.A.* **117**, 26438–26447 (2020).
37. S.hughes, M. van Dop, n. Kolsters, D. van de Klashorst, A. Pogosova, A. M. rijs, Using a *Caenorhabditis elegans* Parkinson's disease model to assess disease progression and therapy efficiency. *Pharmaceuticals* **15**, 512 (2022).
38. J.c. Garcia-Moreno, M. Porta de la riva, e. Martínez-lara, e. Siles, A. cañuelo, Tyrosol, a simple phenol from eVoo, targets multiple pathogenic mechanisms of neurodegeneration in a *C. elegans* model of Parkinson's disease. *Neurobiol. Aging* **82**, 60–68 (2019).
39. B.B. Kautu, A. carrasquilla, M. l. hicks, K. A. caldwell, G. A. caldwell, Valproic acid ameliorates *C. elegans* dopaminergic neurodegeneration with implications for erK-MAPK signaling. *Neurosci. Lett.* **541**, 116–119 (2013).
40. J.Bieschke, J. russ, r. P. Friedrich, D. e. ehrnhoefer, h. Wobst, K. neugebauer, e. e. Wanker, eGcG remodels mature α-synuclein and amyloid-β fibrils and reduces cellular toxicity. *Proc. Natl. Acad. Sci. U.S.A.* **107**, 7710–7715 (2010).
41. T.J. van ham, K. l. Thijssen, r. Breitling, r. M. W. hofstra, r. h. A. Plasterk, e. A. A. nollen, *C.elegans* model identifies genetic modifiers of α-synuclein inclusion formation during aging. *PLOS Genet.* **4**, e1000027 (2008).
42. h. n. currey, A. Malinkevich, P. Melquist, n. F. liachko, ArenA-based activity profiling of tau and TDP-43 transgenic *C. elegans*. *MicroPubl. Biol.* **2020**, 10.17912/micropub. biology.000278 (2020).
43. c. Park, Y. Sakurai, h. Sato, S. Kanda, Y. iino, h. Kunitomo, roles of the clc chloride channel clh-1 in food-associated salt chemotaxis behavior of *C. elegans*. *eLife* **10**, e55701 (2021).
44. D.W. Sanders, S. K. Kaufman, S. l. DeVos, A. M. Sharma, h. Mirbaha, A. li, S. J. Barker, A.c. Foley, J. r. Thorpe, l. c. Serpell, T. M. Miller, l. T. Grinberg, W. W. Seeley, M. i. Diamond, Distinct tau prion strains propagate in cells and mice and define different tauopathies. *Neuron* **82**, 1271–1288 (2014).
45. l. M. A. oliveira, l. J. Falomir-lockhart, M. G. Botelho, K.-h. lin, P. Wales, J. c. Koch, e.Gerhardt, h. Taschenberger, T. F. outeiro, P. lingor, B. Schüle, D. J. Arndt-Jovin, T.M. Jovin, elevated α-synuclein caused by SncA gene triplication impairs neuronal differentiation and maturation in Parkinson's patient-derived induced pluripotent stem cells. *Cell Death Dis.* **6**, e1994 (2015).
46. M.Tada, A. Takeuchi, M. hashizume, K. Kitamura, M. Kano, A highly sensitive fluorescent indicator dye for calcium imaging of neural activity in vitro and in vivo. *Eur. J. Neurosci.* **39**, 1720–1728 (2014).
47. D.S. Knopman, h. Amieva, r. c. Petersen, G. chételat, D. M. holtzman, B. T. hyman, r. A. nixon, D. T. Jones, Alzheimer disease. *Nat. Rev. Dis. Primers* **7**, 33 (2021).
48. i. Domene-Serrano, r. cuadros, V. García-escudero, F. Vallejo-Bedia, i. Santa-María, l. Vallés-Saiz, F. hernandez, J. Avila, Shapeshifter W-Tau peptide inhibits tau aggregation and disintegrates paired helical filaments. *Biochemistry* **64**, 1841–1851 (2025).
49. J.Wang, M. Silva, l. A. haas, n. S. Morsci, K. c. Q. nguyen, D. h. hall, M. M. Barr, *C. elegans* ciliated sensory neurons release extracellular vesicles that function in animal communication. *Curr. Biol.* **24**, 519–525 (2014).
50. K.B. Beer, A. M. Wehman, Mechanisms and functions of extracellular vesicle release in vivo—What we can learn from flies and worms. *Cell Adh. Migr.* **11**, 135–150 (2017).
51. i. Melentijevic, M. l. Toth, M. l. Arnold, r. J. Guasp, G. harinath, K. c. nguyen, D. Taub, J.A. Parker, c. neri, c. V. Gabel, D. h. hall, M. Driscoll, *C. elegans* neurons jettison protein aggregates and mitochondria under neurotoxic stress. *Nature* **542**, 367–371 (2017).
52. A.Fayard, A. Fenyi, S. lavisse, S. Dovero, l. Bousset, T. Bellande, S. lecourtois, c. Jouy, M. Guillermier, c. Jan, P. Gipchtein, B. Dehay, e. Bezard, r. Melki, P. hantraye, r. Aron Badin, Functional and neuropathological changes induced by injection of distinct alpha-synuclein strains: A pilot study in non-human primates. *Neurobiol. Dis.* **180**, 106086 (2023).
53. i. A. nikonorova, J. Wang, A. l. cope, P. e. Tilton, K. M. Power, J. D. Walsh, J. S. Akella, A.r. Krauchunas, P. Shah, M. M. Barr, isolation, profiling, and tracking of extracellular vesicle cargo in *Caenorhabditis elegans*. *Curr. Biol.* **32**, 1924–1936.e6 (2022).
54. J.W. Smit, P. Basile, M. K. Prato, l. Detalle, F.-X. Mathy, A. Schmidt, M. lalla, M. Germani, c. Domange, A.-l. Biere, M. Bani, S. carson, J. Genius, Phase 1/1b studies of UcB0599, an oral inhibitor of α-synuclein misfolding, including a randomized study in Parkinson's disease. *Mov. Disord.* **37**, 2045–2056 (2022).
55. B.Tanudjojo, S. S. Shaikh, A. Fenyi, l. Bousset, D. Agarwal, J. Marsh, c. Zois, S.heman-Ackah, r. Fischer, D. Sims, r. Melki, G. K. Tofaris, Phenotypic manifestation of α-synuclein strains derived from Parkinson's disease and multiple system atrophy in human dopaminergic neurons. *Nat. Commun.* **12**, 3817 (2021).

56. T. Goodpaster, J. randolph-habecker, A flexible mouse-on-mouse immunohistochemical staining technique adaptable to biotin-free reagents, immunofluorescence, and multiple antibody staining. *J. Histochem. Cytochem.* **62**, 197–204 (2014).
57. i. Martinez-Valbuena, G. G. Kovacs, A. e. lang, extracellular vesicles and seeding amplification: A step closer to a Parkinson's disease blood test. *Brain* **145**, 2946–2948 (2022).
58. h. Grosso Jasutkar, S. e. oh, M. M. Mouradian, Therapeutics in the pipeline targeting α-synuclein for Parkinson's disease. *Pharmacol. Rev.* **74**, 207–237 (2022).
59. D. l. Price, M. A. Koike, A. Khan, W. Wrasidlo, e. rockenstein, e. Masliah, D. Bonhaus, The small molecule alpha-synuclein misfolding inhibitor, nPT200-11, produces multiple benefits in an animal model of Parkinson's disease. *Sci. Rep.* **8**, 16165 (2018).
60. c. Z. Baysah, r. A. Dohoney, l. Palanikumar, n. h. Stillman, A. l. Penney, A. D. Sola, D.A. Paredes, M. Magzoub, S. Kumar, A brain-penetrating foldamer rescues Aβ aggregation-associated Alzheimer's disease phenotypes in in vivo models. *ACS Chem. Nerosci.* **16**, 1309–1322 (2025).
61. A.-l. Mougenot, S. nicot, A. Bencsik, e. Morignat, J. Verchère, l. lakhdar, S. legastelois, T.Baron, Prion-like acceleration of a synucleinopathy in a transgenic mouse model. *Neurobiol. Aging* **33**, 2225–2228 (2012).
62. Y. S. Kim, r. i. carp, S. M. callahan, h. M. Wisniewski, incubation periods and survival times for mice injected stereotaxically with three scrapie strains in different brain regions. *J. Gen. Virol.* **68**, 695–702 (1987).
63. A. Surendranathan, l. Su, e. Mak, l. Passamonti, Y. T. hong, r. Arnold, P.Vázquez rodríguez, W. r. Bevan-Jones, S. A. e. Brain, T. D. Fryer, F. i. Aigbirhio, J. B. rowe, J.T. o'Brien, early microglial activation and peripheral inflammation in dementia with lewy bodies. *Brain* **141**, 3415–3427 (2018).
64. l. Antonschmidt, D. Matthes, r. Dervişoğlu, B. Frieg, c. Dienemann, A. leonov, e.nimerovsky, V. Sant, S. ryazanov, A. Giese, G. F. Schröder, S. Becker, B. l. de Groot, c. Griesinger, l. B. Andreas, The clinical drug candidate anle138b binds in a cavity of lipidic α-synuclein fibrils. *Nat. Commun.* **13**, 5385 (2022).
65. S. ray, n. Singh, r. Kumar, K. Patel, S. Pandey, D. Datta, J. Mahato, r. Panigrahi, A. navalkar, S.Mehra, l. Gadhe, D. chatterjee, A. S. Sawner, S. Maiti, S. Bhatia, J. A. Gerez, A.chowdhury, A. Kumar, r. Padinhateeri, r. riek, G. Krishnamoorthy, S. K. Maji, α-Synuclein aggregation nucleates through liquid–liquid phase separation. *Nat. Chem.* **12**, 705–716 (2020).
66. J. e. Galvin, V. M.-Y. lee, J. Q. Trojanowski, Synucleinopathies: clinical and pathological implications. *Arch. Neurol.* **58**, 186–190 (2001).
67. S. Koga, h. Sekiya, n. Kondru, o. A. ross, D. W. Dickson, neuropathology and molecular diagnosis of synucleinopathies. *Mol. Neurodegener.* **16**, 83 (2021).
68. r. i. horne, e. A. Andrzejewska, P. Alam, Z. F. Brotzakis, A. Srivastava, A. Aubert, M. nowinska, r. c. Gregory, r. Staats, A. Possenti, S. chia, P. Sormanni, B. Ghetti, B.caughey, T. P. J. Knowles, M. Vendruscolo, Discovery of potent inhibitors of α-synuclein aggregation using structure-based iterative learning. *Nat. Chem. Biol.* **20**, 634–645 (2024).
69. A. Ugarte, D. corbacho, M. S. Aymerich, A. García-osta, M. cuadrado-Tejedor, J. oyarzabal, impact of neurodegenerative diseases on drug binding to brain tissues: From animal models to human samples. *Neurotherapeutics* **15**, 742–750 (2018).
70. A. Morales-Kastresana, B. Telford, T. A. Musich, K. McKinnon, c. clayborne, Z. Braig, A.rosner, T. Demberg, D. c. Watson, T. S. Karpova, G. J. Freeman, r. h. DeKruyff, G.n. Pavlakis, M. Terabe, M. robert-Guroff, J. A. Berzofsky, J. c. Jones, labeling extracellular vesicles for nanoscale flow cytometry. *Sci. Rep.* **7**, 1878 (2017).
71. l. Ferrari, S. G. D. rüdiger, recombinant production and purification of the human protein Tau. *Protein Eng. Des. Sel.* **31**, 447–455 (2018).
72. o. Margie, c. Palmer, i. chin-Sang, *C. elegans* chemotaxis assay. *J. Vis. Exp.* **2013**, 50069 (2013).
73. J. chaudhuri, M. Parihar, A. Pires-daSilva, An introduction to worm lab: From culturing worms to mutagenesis. *J. Vis. Exp.* **2011**, 2293 (2011).
74. A. J. harrington, T. A. Yacoubian, S. r. Slone, K. A. caldwell, G. A. caldwell, Functional analysis of VPS41-mediated neuroprotection in *Caenorhabditis elegans* and mammalian models of Parkinson's disease. *J. Neurosci.* **32**, 2142–2153 (2012).
75. r. A. Dohoney, J. A. Joseph, c. Baysah, A. G. Thomas, A. Siwakoti, T. D. Ball, S. Kumar, "common-Precursor" protein mimetic approach to rescue Aβ aggregation-mediated Alzheimer's phenotypes. *ACS Chem. Biol.* **18**, 1510–1522 (2023).
76. Y. Sun, P. e. Arslan, A. Won, c. M. Yip, A. chakrabartty, Binding of TDP-43 to the 3′UTr of its cognate mrna enhances its solubility. *Biochemistry* **53**, 5885–5894 (2014).
77. Y. You, S. Muraoka, M. P. Jedrychowski, J. hu, A. K. McQuade, T. Young-Pearse, r. Aslebagh, S.A. Shaffer, S. P. Gygi, M. Blurton-Jones, W. W. Poon, T. ikezu, human neural cell type-specific extracellular vesicle proteome defines disease-related molecules associated with activated astrocytes in Alzheimer's disease brain. *J. Extracell. Vesicles* **11**, e12183 (2022).
78. M. Barth, M. Bacioglu, n. Schwarz, r. novotny, J. Brandes, M. Welzer, S. Mazzitelli, l. M. häsler, M. Schweighauser, T. V. Wuttke, D. Kronenberg-Versteeg, K. Fog, M. Ambjørn, A.Alik, r. Melki, P. J. Kahle, D. r. Shimshek, h. Koch, M. Jucker, G. Tanriöver, Microglial inclusions and neurofilament light chain release follow neuronal α-synuclein lesions in long-term brain slice cultures. *Mol. Neurodegener.* **16**, 54 (2021).
79. e. G. oldani, n. h. Stillman, r. A. Dohoney, c. Z. Baysah, S. Kumar, inhibition of phosphorylated alpha-synuclein aggregation by synthetic protein mimetics and foldamers. *ACS Chem. Nerosci.* **16**, 152–160 (2025).
80. l. Di, e. h. Kerns, Y. hong, h. chen, Development and application of high throughput plasma stability assay for drug discovery. *Int. J. Pharm.* **297**, 110–119 (2005).
81. i. Kariv, h. cao, K. r. oldenburg, Development of a high throughput equilibrium dialysis method. *J. Pharm. Sci.* **90**, 580–587 (2001).
82. S. J. enna, Goodman & Gilman's *The Pharmacological Basis of Therapeutics* edited by Joel G.hardman, lee e. limbird, Perry B. Molinoff, and raymond W. ruddon. McGraw-hill, new York. 1996. xxi + 1905 pp. 21 × 26 cm. iSBn 0-07-026266-7. $89.00. *J. Med. Chem.* **40**, 2657–2658 (1997).
83. l. Palanikumar, l. Karpauskaite, M. Al-Sayegh, i. chehade, M. Alam, S. hassan, D. Maity, l. Ali, M. Kalmouni, Y. hunashal, J. Ahmed, T. houhou, S. Karapetyan, Z. Falls, r. Samudrala, r. Pasricha, G. esposito, A. J. Afzal, A. D. hamilton, S. Kumar, M. Magzoub, Protein mimetic amyloid inhibitor potently abrogates cancer-associated mutant p53 aggregation and restores tumor suppressor function. *Nat. Commun.* **12**, 3962 (2021).
84. l. Palanikumar, S. Al-hosani, M. Kalmouni, V. P. nguyen, l. Ali, r. Pasricha, F. n. Barrera, M. Magzoub, ph-responsive high stability polymeric nanoparticles for targeted delivery of anticancer therapeutics. *Commun. Biol.* **3**, 1–17 (2020).
85. S. A. Flowers, l. Ali, c. S. lane, M. olin, n. G. Karlsson, Selected reaction monitoring to differentiate and relatively quantitate isomers of sulfated and unsulfated core 1 o-glycans from salivary MUc7 protein in rheumatoid arthritis. *Mol. Cell. Proteomics* **12**, 921–931 (2013).
86. S. lohmann, J. Grigoletto, M. e. Bernis, V. Pesch, l. Ma, S. reithofer, G. Tamgüney, ischemic stroke causes Parkinson's disease-like pathology and symptoms in transgenic mice overexpressing alpha-synuclein. *Acta Neuropathol. Commun.* **10**, 26 (2022).
87. B. M. Slotnick, c. M. leonard, *A Stereotaxic Atlas of the Albino Mouse Forebrain* (U.S. Department of health, education, and Welfare, Public health Service, Alcohol, Drug Abuse, and Mental health Administration, 1975).
88. c. Perry, J.-Y. chung, K. Ylaya, c. h. choi, A. Simpson, K. T. Matsumoto, W. A. Smith, S.M. hewitt, A buffered alcohol-based fixative for histomorphologic and molecular applications. *J. Histochem. Cytochem.* **64**, 425–440 (2016).

Acknowledgments: We thank the Department of chemistry and Biochemistry, the Knoebel institute for healthy Aging, and the University of Denver (DU) for startup support. We are grateful to M. Diamond (University of Texas Southwestern Medical center, Dallas, TX, USA) for heK cells and to G. caldwell (Department of Biological Sciences, University of Alabama, Tuscaloosa, Al, USA) for the UA196 worms. We also thank A. Darehshouri at cU Anschutz for assistance with TeM imaging supported by the electron Microscopy core Facility at cU Anschutz. Data were collected using the Jeol JeM-120i, 120 kV TeM, supported by nih grant 1S10oD036258-01. **Funding:** This project was funded by the American Parkinson's Disease Association r79 (to S.K.), the Parkinson's Foundation PF-SF-JFA-1046268 (Stanley Fahn Junior Faculty award to S.K.), nih-ninDS (1r61nS137824-01) (to S.K.), a Movement Disorders Foundation grant (to S.K.), a Movement Disorders Foundation postdoctoral grant (to e.o.), Mcin/Aei/10.13039/501100011033 FeDer and eU research grant PiD2022-136997nB-i00 (both to n.c.), the colorado Department of Public health and environment 17-90046, rFA-1353 (to M.l.), an nYU Abu Dhabi research grant (AD389), and an ADeK ASPire Award (AAre20-371) (both to M.M.), and inAMeS - MDc-Weizmann helmholtz international research School for imaging and Data Science from the nAno to the MeSo (to P.S.o.). **Author contributions:** conceptualization of the project was carried out by S.K. and M.M. Synthesis of SK-129 and its analogs was carried out by r.A.D. Biophysical assays were performed by J.A.J., n.h.S., r.A.D., e.o., T.D.B., K.M.r.c., T.c.F., and J.A. cellular studies and imaging were performed by e.o., P.c., and T.D.B. neuron studies we carried out by P.S.o., and FliM and single-molecule fluorescence analysis were performed by D.P. and n.c. Pharmaceutical properties investigation was performed by n.h.S., and *C. elegans* studies and imaging were performed by J.A.J. and c.Z.B. The mouse studies were performed by l.P. original draft was written by S.K. and revisions/editing were done with all other authors. **Competing interests:** This work has been filed for a patent application (international patent no.: Wo/2025/006818) by DU (lead institute) and nYU at Abu Dhabi. S. Kumar and r.A. Dohoney from DU and M. Magzoub and P.l. from nYU Abu Dhabi are the inventors of the patent. The remaining authors declare that they have no competing interests. **Data, code and materials availability:** All data associated with this study are present in the paper or the Supplementary Materials. All the datasets generated and analyzed during the current study and raw data are also available from the corresponding author upon request. The foldamer SK-129 can be made available to interested researchers through a material transfer agreement with DU (email: sunil.kumar97@du.edu). All other materials used or generated in this study are commercially available or will be supplied upon reasonable request.